GU-68

Working Paper No. 11

December 2, 1963

RELIABILITY ANALYSIS OF THE CENTAUR IGS FIRST GIMBAL STABILIZATION LOOP

Prepared by

W. S. Connor and W. S. Thompson

Prepared for
National Aeronautics and Space Administration
under
Contract No. NASw-334

Table of Contents

		Page
	List of Symbols	ii
	List of Tables	v
	List of Figures	vi
I.	Introduction and Summary	One
II.	Definition of the System Mission	Five
III.	Equipment Description	Eleven
IV.	Functional Description	Twelve
V.	System Functional Analysis	Thirteen
VI.	Statistical Analysis	Twenty-Five
VII.	Acknowledgment	Thirty-Three
	References	Thirty-Five

LIST OF PRINCIPAL SYMBOLS

a_{IA} - True vehicle acceleration along the gyro IA

a_{SRA} - True vehicle acceleration along the gyro SRA

a_U, a_V - True accelerations along the U_i, V_i inertial axes

a_U^*, a_V^* - Accelerations measured along the U_o, V_o platform axes.

CT - Same as α_1

e_{A1} - Output voltage of the first stage of amplification in the GCA

e_{A2} - Output current of the second stage of amplification in the GCA

e_c - Output voltage of the system compensation network

e_d - Null output current of the GCA

e_p - Output voltage of the preamplifier

e_S - Output voltage of the gyro signal generator

f - Combined total viscous damping coefficient of the torque motor, slip rings and gimbal bearings

$f_c(s)$ - Normalized transfer function of the system compensation network

F - Combined non-linear Coulomb and break-away friction

$F(j\omega)$ - System frequency response function

F(s) - System transfer function

g - Acceleration due to gravity (32.2 ft./sec.^{2})

GCA - Abbreviation for "Gimbal Control Amplifier"

H - Angular momentum of the gyro rotor

$\underline{I}$ - Symbolic representation of a fixed set of system input conditions under which the reliability is estimated.

I - Moment of inertia of the gyro gimbal about the gyro OA

IA - Abbreviation for "Gyro Input Axis"

IGS - Abbreviation for "Inertial Guidance System"

j - $\sqrt{-1}$

J - Moment of inertia of the gyro gimbal about the gyro OA

k_c - Static gain of the system compensation network

k_{A1} - Effective DC static gain of the first stage of amplification in GCA

k_{A2} - Effective DC static gain of the second stage of amplification in the GCA

k_M - Effective static gain or sensitivity of the torque motor

k_p - Effective DC static gain of the preamplifier

k_s - Effective DC static gain of the gyro signal generator

$\mathcal{L}$ - Laplace operator

MUIA - Same as α_2

MUSRA - Same as α_3

OA - Abbreviation for "Gyro Output Axis"

$\vec{r}$ - Vehicle range vector measured from earth's center

$\vec{r}_E$ - Earth's radius vector

R - Reliability

s - Laplace variable

SRA - Abbreviation for "Gyro Spin Reference Axis"

t - Time

T_d - Sum of all disturbing torques acting on the platform gimbal

T_f - Gimbal disturbing torque resulting from viscous friction

T_F - Gimbal disturbing torque resulting from the non-linear Coulomb and break-away friction

T_M - Servo control torque delivered by the torque motor

T_n - Net torque acting on the platform gimbal

T_R - Gyro reaction torque acting on the platform gimbal

U_E, V_E, W_E - Axes of the true inertial reference frame with the origin at earth's center

U_i, V_i, W_i - Axes of the true inertial reference frame with the origin centered on the stable platform

U_o, V_o, W_o - Axes of the stable platform

$\vec{v}$ - Vehicle velocity vector

V_U - Actual vehicle crossrange velocity along the U_i axis

$V_{U\epsilon}$ - Vehicle crossrange velocity error

V_U^* - Vehicle crossrange velocity along the U_i axis computed from measured acceleration

V_U', V_U'' - Failure bounds on $V_U(T_1)$

x(t) - Random process

α_1 - Gyro drift rate due to constant torques

α_2 - Gyro drift rate due to mass unbalance along the gyro IA

α_3 - Gyro drift rate due to mass unbalance along the gyro SRA

β_1, β_2 - Gyro drift rate coefficients

γ_o, γ_1 - GCA drift coefficients

$\Delta\alpha_1$ - Residual gyro drift rate due to constant torques after drift compensation

$\Delta\alpha_2$ - Residual gyro drift rate due to mass unbalance along the gyro IA after drift compensation

$\Delta\alpha_3$ - Residual gyro drift rate due to mass unbalance along the gyro SRA after drift compensation

θ - Angular deflection of the gyro gimbal about the gyro OA

$\dot{\theta}_d$ - Residual drift rate of the gyro after drift compensation

Φ - Power spectral density

Ψ_e - Platform error angle or the angle between the true inertial reference and the reference established by the platform

Ψ_e', Ψ_e'' - Failure bounds on $\Psi_e(T_2)$

Ψ_i - Inertial angular orientation of the vehicle or the angle between the true inertial reference and the vehicle reference

Ψ_o - Angle between the platform reference and the vehicle reference

ω - Angular frequency in rad./sec.

LIST OF TABLES

		Page
Table I.	Estimation of the Variance of MUSRA, (α_3), for a Particular Gyro	Thirty-Six
Table II.	Estimated Variances of CT, MUIA, and MUSRA for All Gyros	Thirty-Seven
Table III.	Estimates of β_1 and β_2 and Associated Variances	Thirty-Eight
Table IV.	Estimation of the Between Gyros Component of Variance of β_1	Thirty-Nine
Table V.	Estimated Variances, Covariances and Correlation	Forty

LIST OF FIGURES

		Page
Figure 1.	Simplified Description of Vehicle Mission	Forty-One
Figure 2.	Major Sequential Stages of System Operation	Forty-One
Figure 3.	Geometry for an Ideal Stable Platform	Forty-Two
Figure 4.	Effect of Platform Azimuth Drift on Measured Accelerations	Forty-Three
Figure 5.	Dynamic Representation of Single-Axis Stabilization Loop	Forty-Four
Figure 6.	Operational Profile for Vehicle Angular Motion About the W_i Axis	Forty-Five
Figure 7.	Closed Loop Response of a Linear Feedback System	Forty-Six
Figure 8.	Gyro Orientation in the Platform	Forty-Seven
Figure 9.	Mission Acceleration Profile	Forty-Eight
Figure 10.	Illustration of Measurements of Gyro Drift Variables CT, MUIA or MUSRA	Forty-Nine
Figure 11.	Six Minute Averages of Gyro Drift Rate and a Fitted Trend Line	Fifty
Figure 12.	Scatter Plot of MUSRA vs. MUIA for One Gyro	Fifty-One
Figure 13.	Linear and Quadratic Coefficients, Plotted on Normal Probability Paper	Fifty-Two
Figure 14.	Estimated Drift Reliability, As a Function of the Allowable Error in Velocity at the End of Boost $V_U(T_1)$	Fifty-Three
Figure 15.	Probability That the Platform Drift is Within the Allowable Error at the End of Orbit	Fifty-Four

RELIABILITY ANALYSIS OF THE CENTAUR IGS FIRST GIMBAL STABILIZATION LOOP

I. Introduction and Summary

A. General

In the current effort to develop new techniques for predicting the reliability of complex systems, a fundamental and theoretical probabilistic model for systems reliability was developed and presented in [1]. In a reliability analysis of a system, this model provides a framework for consideration of all system variables that affect the reliability of the system.

The general acceptance of any new theory or technique depends largely on the degree of success in application to problems of immediate concern. To promote the acceptance of the newly-developed reliability model, the techniques are demonstrated by application to a system selected for analysis. Due to the current interest in space systems, the system selected for this demonstration is an inertial guidance system of a space vehicle. It was considered advantageous to consider a specific system, permitting a firm definition of all system parameters and equipment. For this purpose, the CENTAUR IGS (Inertial Guidance System), manufactured by the Minneapolis-Honeywell (MH) Regulator Company in St. Petersburg, Florida, was designated as a typical system. Whereas the analysis is limited to this specific system, no loss results in the generality of the model for application to other inertial guidance systems or systems of other types.

The current analysis of the CENTAUR IGS was initiated with [2] wherein it was proposed to limit the analysis to a subsystem of the CENTAUR IGS, viz., the azimuth gimbal stabilization loop of the CENTAUR IGS stable platform. Again this simplification results in no loss of generality since the instrumentation and functional operation are sufficiently complex to introduce the application of the new techniques presented by the reliability model.

Some additional analysis was presented in [3] which required a security classification of CONFIDENTIAL due to the inclusion of certain system specifications in that report. A detailed description of the functional operation of a single axis stabilization loop was presented in [4] for the benefit of those persons interested in this analysis but who are unfamiliar with the operation of stable platforms and control systems.

The purpose of this report is to present the final phase of the analysis of the selected system. Simplifications are frequently introduced to permit the convenient use of pure analytical techniques instead of numerical techniques which would entail much expense and time for digital computation. Since the primary objective in this analysis is to develop and demonstrate new methodology, the simplifications are not considered seriously detrimental to this purpose. When conducted jointly with a systems development program where extensive digital computer facilities are available, these simplifications would not be required.

To some readers it may also appear initially that an extraordinary amount of analysis is required to obtain the relatively simple results presented; however, a major portion of the analysis presented is identical to that already required of systems engineers during the design and development stage of a system to analyze the system performance. Since reliability inherently encompasses all performance measures of a system, it is highly advocated that reliability analysis and control should become an integral part of the overall program task performed by systems engineers. This is not intended to deemphasize the tasks of the reliability engineer who plays an increasingly important role in controlling such factors as design and production techniques and component selection; rather, dissemination of the theory included in the reliability model by these individuals would greatly enhance their ability to make sound decisions.

As a result of the security classification of the selected system, it is necessary to publish the results of this analysis in a coded form; therefore, <u>the results of this analysis are in no way considered to reflect the operational reliability of the CENTAUR IGS</u>.

B. Summary

The contents of this report are as follows. A typical, but somewhat simplified system mission, is described, and success of the mission is defined in terms of suitable criteria. It is then desired to estimate the probability that a flight will be successful. The equipment required to instrument functional requirements and a functional description of the system have been described in other reports, which are referenced below.

It is emphasized in the report that any estimate of reliability is dependent on the conditions under which tests are carried out and on the kind and quantity of data which are generated by the tests. The data available for the present analysis were collected from tests conducted during manufacturing, and hence do not reflect mission conditions. Also, the only element for which degradation was recorded as a function of time was the gyro, so that the drift reliability analysis of the loop depended principally on gyro drift rate data.

In the analysis conducted in this report, no estimate is made of the probability of the catastrophic failure of the stabilization loop; only drift failure is considered. Although a complete analysis would require that both types of failure be considered, the authors feel that the probability of drift failure is much higher than that of catastrophic failure for the system considered. In addition, because conventional reliability analysis usually ignores the drift behavior of systems and a basic facet of the methodology under development is to take account of drift behavior when it is important, the present report is devoted to the analysis of drift behavior.

The statistical analysis is described in the last section of this report. It consists principally of utilizing gyro test data to estimate the reliability of the system. Linear functions of several random variables determine the performance of the system. Their variances are estimated and, by use of normal theory, estimates of reliability are obtained.

To avoid the necessity of classifying this report, the Tables referred to in the last section are shown only in format, without numbers. The numbers are available under separate cover in a classified report.

The study reported in [5] serves as background for the present report. It summarizes the test and data collection procedures employed by MH in the production of the CENTAUR IGS.

II. Definition of the System Mission

The analysis of any system begins with a definition of the system mission and a specification of the functions that the system must perform to successfully complete the mission. This subsequently leads to a definition of the hardware for instrumenting the required functions and finally a recognition of the variables and processes involved which are apt to effect failure or degraded performance of the system.

The single-axis stabilization loop, selected for the reliability analysis herein, is a subsystem of a large space vehicle system. The mission of the complete vehicle system is first defined.

A typical mission of a space vehicle system for consideration is the launch and delivery of a payload, e.g., a space probe, to a distant celestial object, say, the planet Mars as illustrated in Figure 1. The mission begins at time $t = 0$ with the initiation of a boost phase and ends at $t = T_4$ with arrival at the target. Several stages of sequential system operation are required for the mission and are more clearly identified in Figure 2.

The criteria for success of the mission may be based on certain conditions to be obtained at T_4. For example, a successful soft landing of the payload on Mars entails certain accuracy requirements on such factors as landing position, velocity at impact and orientation of the spacecraft. Achievement of these requirements depends upon the successful performance of all previous functions in the four sequential stages of operation specified. Specifically, the accuracy in the landing position is dependent upon the velocity and the position vectors of the spacecraft at time T_3, the time of final thrust cutoff for the launch vehicle. Similarly, the velocity and position at T_3 are related to previous performance of the system and, definitely, to the single axis stabilization loop to be analyzed.

The performance of the loop affects the operation of all stages; however, with sufficient foreknowledge of the loop operation, the contribution of loop degraded performance to the over-all system performance is recognizably distinct for two phases of flight, (1) the power phase where the loop experiences thrust accelerations and (2) the coast phase where the net acceleration on the loop is zero. The power phase of flight is represented by the two boost stages I and III illustrated in Figure 2 and the coast

phase by the orbit stage, stage II, and the space trajectory stage, stage IV. Due to this similarity between the stage pairs, the reliability analysis techniques are sufficiently demonstrated by limiting the analysis to stages I and II.

The functional requirements of the single-axis stabilization loop as they relate to the over-all system operation are identified for stages I and II below.

Stage I - Boost into Orbit

The function of the overall vehicle system is to launch the upper stage of the vehicle (which contains the payload) into a parking orbit around the earth. Prior to launch, a desired parking orbit will be known, the establishment of which requires a certain velocity vector and altitude of the vehicle thrust cutoff (time T_1). Achievement of the velocity and altitude conditions is accomplished by vehicle guidance.

Vehicle guidance is instrumented by physically controlling the direction of the vehicle thrust according to some preconceived navigation law. Computation of the navigation law during flight requires continuous knowledge of vehicle velocity and position. For an inertial guidance system as considered for this application both velocity and position are computed from measured vehicle accelerations.

Solution of the guidance law is performed using inertial coordinates; therefore, the vehicle acceleration must also be measured in inertial coordinates. The stable platform is provided in the vehicle as a space (inertial) stabilized mounting block for the accelerometers.

An ideal stable platform mounted in the vehicle would provide a space stabilized coordinate system as illustrated in Figure 3 by the mutually orthogonal platform axes U_i, V_i, W_i. At launch (position 1) the W_i axis is aligned coincident with local vertical or the earth's radius vector $\vec{r}_E$. The V_i axis is aligned horizontal in the desired flight direction with the U_i axis aligned horizontal and orthogonal to V_i and W_i to form a righthanded coordinate system as shown. The V_i, W_i plane is defined as the desired flight plane containing the vehicle trajectory.

During flight (position 2), at some time after launch, the vehicle has a range $\vec{r}$ and velocity $\vec{v}$ in the inertial (but earth centered) frame of reference formed by the U_E, V_E, W_E axes. The orientation of the U_i, V_i, W_i coordinate system provided by the ideal platform remains fixed, as shown, even though the vehicle structure rotates with respect to inertial space.

The actual stable platform for providing a space stabilized frame of reference is a four gimbal configuration with a separate control loop provided for each gimbal [6]. The complete instrumented platform establishes three axes U_o, V_o, W_o which, for perfect operation of the control loops, are mutually orthogonal and coincident with respective axes U_i, V_i and W_i providing the desired space stabilized frame of reference.

The single-axis stabilization loop considered for analysis is the control loop for the inner or first gimbal which is the stable platform proper. The axis of rotation of the platform or first gimbal is defined as the W_o axis.

The primary functional requirement of the single-axis stabilization loop during stage I system operation is to provide a stable mounting for the accelerometers about the W_o axis of rotation. The three outer gimbals of the four gimbal platform configuration isolate the first gimbal from rotation about the U_o and V_o axes so that the operation of the single-axis stabilization loop for the first gimbal in providing angular stabilization about the W_o axis is similar to that of a single-axis platform, the basic operation of which has been thoroughly defined [4].

Since the function of the loop is to maintain a stable inertial reference, degraded performance of the stabilization loop is characterized solely by the platform drift resulting from disturbances introduced into the loop and drift of the various components within the loop. The effect of the drift on the measured acceleration is shown in Figure 4. Drift about the W_i (or W_o) axis is denoted by Ψ_e, the angle between the true inertial axes and the platform axes as shown. Assuming perfect accelerometers and precise alignment of their input axes along the U_o and V_o platform axes, the accelerations measured along these axes are

$$a_U^* = a_U \cos \Psi_e + a_V \sin \Psi_e \tag{1}$$

and

$$a_V^* = a_V \cos \Psi_e - a_U \sin \Psi_e \tag{2}$$

where a_U^* and a_V^* are the measured accelerations along the U_o and V_o axes respectively and a_U and a_V are the true accelerations along the U_i and V_i axes.

Reasonably good loop performance usually yields only small angles of Ψ_e. Assuming, then, only small angles for Ψ_e,

$$\sin \Psi_e \simeq \Psi_e \text{ (in radians)}; \cos \Psi_e \simeq 1 \ . \tag{3}$$

Furthermore, since the desired flight direction is chosen along the V_i axis as shown in Figure 3, a_U is the crossrange acceleration which is always small compared to a_V. Incorporating this condition along with those of (3), (1) and (2) effectively reduce to

$$a_U^* \simeq a_U + a_V \Psi_e \tag{4}$$

and

$$a_V^* \simeq a_V \ . \tag{5}$$

Thus the platform drift affects primarily the crossrange acceleration a_U.

In the instrumentation of the vehicle guidance the velocity components are the major inputs to the guidance computer for computing the vehicle steering signals. To obtain the velocity inputs each accelerometer output is integrated, and for the crossrange, velocity instrumentation of the integration provides

$$V_U^*(t) = \int_o^t a_U^*(\tau), \, d\tau \ , \tag{6}$$

where $V_U^*(t)$ is the computed vehicle crossrange velocity and t is time with τ introduced as the dummy time variable of integration. a_U^* is also expressed in (6) as a function of time, $a_U^*(t)$, since the variables in (4) are functions of time; $a_U(t)$ and $a_V(t)$ are determined by the mission acceleration profile and $\Psi_e(t)$ results from the behavior of the single-axis stabilization loop.

Substituting (4) into (6) and integrating term by term

$$V_U^*(t) = \int_o^t a_U(\tau)\, d\tau + \int_o^t a_V(\tau)\, \Psi_e(\tau)\, d\tau$$

$$= V_U(t) + \int_o^t a_V(\tau)\, \Psi_e(\tau)\, d\tau \ , \tag{7}$$

where $V_U(t)$ is the actual crossrange velocity of the vehicle. The error $V_{U\epsilon}$ in the computed crossrange velocity is

$$V_{U\epsilon}(t) = V_U^*(t) - V_U(t) = \int_o^t a_V(\tau)\, \Psi_e(\tau)\, d\tau \ . \tag{8}$$

The V_i, W_i plane was defined, in connection with Figure 3, as the desired flight plane or the plane containing the trajectory, and the orientation of the platform prior to launch places this plane in the desired flight direction. Crossrange guidance attempts to maintain the vehicle in the V_i, W_i plane throughout flight or more specifically to provide at the end of boost

$$V_U(T_1) = 0 \ ,$$

which is a desirable condition for establishing the predetermined parking orbit. However, the vehicle steering signals are computed with $V_U^*(t)$, and with this input to the guidance computer the control system now attempts to provide

$$V_U^*(T_1) = 0 \ . \tag{9}$$

Substituting the condition of (9) into (8) and setting $t = T_1$ to obtain the crossrange velocity error at the end of boost,

$$V_{U\epsilon}(T_1) = -V_U(T_1) = \int_o^{T_1} a_V(\tau)\, \Psi_e(\tau)\, d\tau \ . \tag{10}$$

Therefore, assuming perfect response of the vehicle control system to the computed steering signals, the vehicle velocity error due to platform drift about the W_o axis is the negative of the actual crossrange velocity $V_U(T_1)$.

In establishing the parking orbit, $V_U(T_1)$ affects primarily the angle of inclination of the orbit with the equator. The allowable error in this angle will determine the allowable error or failure bounds on $V_U(T_1)$ such that the conditions for success of the single-axis stabilization loop at time T_1 can be stated as

$$V_U' \leq V_U(T_1) \leq V_U'' \ . \tag{11}$$

Stage II - Parking Orbit

The stable platform is located in the upper stage of the vehicle which is injected into orbit by the booster. Having established the parking orbit, the platform control system continues to operate with the assigned function of maintaining a stable inertial reference.

Resolvers located at the ends of the platform gimbal axes provide electrical signal outputs which are used to compute the orientation of the vehicle with respect to the inertial reference provided by the platform. This may be required in order to keep the vehicle oriented in some prescribed direction throughout the parking orbit.

Considered of major importance for the analysis herein is the accumulative drift of the platform at the end of the parking orbit (time T_2) since this drift affects the initial orientation or pointing direction of the vehicle for the start of the power flight in stage III and subsequently the guidance accuracy during stage III and the space trajectory following. The accumulative drift of the platform about the W_o axis is $\Psi_e(T_2)$ as provided by the single-axis stabilization loop.

The conditions for success of the single-axis stabilization loop at time T_2 are

$$V_U' \leq V_U(T_1) \leq V_U'' \text{ and } \Psi_e' \leq \Psi_e(T_2) \leq \Psi_e'' \ . \tag{12}$$

III. Equipment Description

The equipment required to instrument the functional requirements of the single-axis stabilization loop for the prescribed mission are identified in the system schematic diagram presented in [2]. Each component identified in that representation was originally designated as a system element for the analysis; however, later consideration of the loop in [3] permitted elimination of certain elements and recombinations of others to form a loop of seven (7) elements. These loop elements are again listed below for further reference in the analysis.

Element Number	Element Name
1	Gyro
2	Preamplifier
3	Slip ring
4	GCA (Gimbal Control Amplifier)
5	Slip ring
6	Torque motor
7	Gimbal

IV. Functional Description

After simplification of the loop and identification of the available data for possible use in a reliability analysis, a functional diagram of the loop was constructed and presented in [5], Figure 6. This functional description reveals the interrelationships among the loop elements and the inputs to the elements from external sources. The major sources of inherent loop degradation are identified by the two attributes $\dot{\theta}_d$, the residual gyro drift rate after drift compensation and e_d, the GCA null current.

V. System Functional Analysis

A. Loop Reliability Defined

The reliability R(t) of the single-axis stabilization loop during the mission defined earlier is

$$R(t) = \text{Prob}\ \{\text{no failure in } (0,t)\} \tag{13}$$

where, as indicated in Figure 2, the mission begins at vehicle launch or $t = 0$. The accuracy requirements of the loop for operational stages I and II were stated by (11) and (12).

For analysis the allowable range of variation for $V_U(T_1)$ and $\Psi_e(T_2)$ are assumed equivalent in both positive and negative directions so that the criteria for success may be stated as $|V_U(T_1)| \leq V_U'$ and $|\Psi_e(T_2)| \leq \Psi_e'$. The reliability of the loop at the end of boost is then defined by

$$R(T_1) = \text{Prob}\ \{|V_U(T_1)| \leq V_U'\}\ , \tag{14}$$

and at the end of the parking orbit

$$R(T_2) = \text{Prob}\ \{|V_U(T_1)| \leq V_U' \text{ and } |\Psi_e(T_2)| \leq \Psi_e'\} \tag{15}$$

The probability measures in (14) and (15) define the reliability of the single-axis stabilization loop at two points in time during the mission with the inherent assumption that the system is exposed to the true mission conditions defined by the mission operational profile.

In the reliability analysis, it is desirable to estimate the above probability measures. The approach employed in this analysis is to predict the reliability on the basis of the observed behavior of each individual element in the loop. Assuming that data which reflects the behavior of each element is available, the purpose of the analysis, then, is to combine the data using the functional relationships of the loop and the elements, while also employing necessary statistical techniques, to obtain the predicted behavior of the loop.

An investigation of the CENTAUR IGS manufacturing process has been conducted to determine the availability of useful data for analysis in predicting the reliability of the single-axis stabilization loop. This

investigation is described in detail and the available data identified in [5]. The scope of the investigation was restricted to the data and test procedures being employed in the production phase of the product cycle, and, as anticipated, the type of data required for the reliability analysis was limited in quantity. During the production phase of the product cycle as studied, tests are conducted at practically all levels of system assembly. The primary purpose of the tests is to insure that the final assembly of the system conforms to assigned customer specifications.

Gyro drift data was identified as the available data most pertinent to the analysis. Static friction data on the slip rings and torque motor was also obtained. Drift data for the GCA was desired but was not available; however, GCA drift is assumed in the analysis by using artificial data to illustrate that the effect can be included.

The observed behavior of any element during a test is dependent upon the input conditions under which the element is tested. The majority of tests during the production phase are conducted under conditions of controlled fixed inputs. A general breakdown of the different types of inputs offered in [5] was: 1) informational (e.g., input signals), 2) operational (e.g., required power supply inputs) and 3) environmental (e.g., temperature stress level). For a given test the informational inputs are usually specified at some convenient fixed level within the normal operating range, the operational inputs are set at the nominal design value and the environmental inputs are fixed at laboratory or room conditions unless intentional overstressing, such as operation at elevated temperatures, is employed.

Use of data, obtained under such controlled conditions, in a reliability analysis does not permit a prediction of the mission reliability since the test conditions do not simulate the mission operational profile. Any reliability prediction ventured with such data must be recognized as conditioned on the specific test conditions. As provided in the reliability model of [1], the reliability may be defined to reflect the condition. Letting $\underline{I}$ symbolically represent the specific input conditions under which the element behaviors are observed, conditional reliabilities are defined as

$$R(T_1|\underline{I}) = \text{Prob}\ \{|V_U(T_1)| \leq V_U'|\ \underline{I}\} \tag{16}$$

and

$$R(T_2|\underline{I}) = \text{Prob}\ \{|V_U(T_1)| \leq V_U' \text{ and } |\Psi_e(T_2)| \leq \Psi_e'|\ \underline{I}\} \tag{17}$$

which are the probability measures to be estimated.

B. Loop Behavior Over Time

To estimate the probability measures of (16) and (17) it is necessary to relate the variables $V_U(T_1)$ and $\Psi_e(T_2)$ to the observed performance attributes of the elements. This is accomplished with the functional relationships of the loop.

A detailed functional description of the loop was presented in [4] with the complete dynamic representation of the loop defined by Figure 10 of that report. This diagram is reproduced with several alterations in Figure 5 of this report with all symbols defined in the accompanying list at the front of this report. The major changes introduced into this representation is replacement of the U disturbing torques about the gyro output axis by the equivalent residual gyro drift rate $\dot{\theta}_d$ caused by the disturbing torques and inclusion of an additional input disturbance e_d to represent the GCA null current.

The loop output is $\Psi_e(s)$ and is a function of $\dot{\Psi}_i(s)$, $e_d(s)$ and $\dot{\theta}_d(s)$. If the Coulomb friction level F (also assumed to represent the static or break-away friction level) of the torque motor and slip rings combined is small, this functional relationship is linear; however, with F significantly large, the functional relationship becomes a complicated non-linear relationship.

$\Psi_e(s)$ represents a complex frequency response of the loop, and to obtain $V_U(T_1)$ and $\Psi_e(T_2)$ as needed for the reliability prediction, it is necessary to determine an equivalent time response $\Psi_e(t)$[1] as a function of $\dot{\Psi}_i(t)$, $e_d(t)$ and $\dot{\theta}_d(t)$. A standard technique for obtaining the time response of complex non-linear systems is simulation. An attempt was made to set up and conduct a dynamic simulation of the loop on an analog computer

---

[1]The convention employed herein is to let x(s) represent the Laplace transform of x(t), i.e., $x(s) = \mathcal{L}[x(t)]$ and $x(s) \neq x(t)|_{t=s}$.

to include the non-linear effects caused by F; however, it was discovered that the computer and the required simulation program were not compatible. At that project stage, time did not permit reprogramming for a digital computer simulation, therefore the logical alternative was to restrict the study to analysis of a linear system.

The linear closed loop complex frequency response of the system to disturbing inputs $\dot{\Psi}_i(s)$, $\dot{\theta}_d(s)$ and $e_d(s)$ is expressed by

$$\Psi_e(s) = F_1(s)\,\dot{\Psi}_i(s) + F_2(s)\,\dot{\theta}_d(s) + F_3(s)\,e_d(s)\ , \tag{18}$$

or

$$\Psi_e(s) = \Psi_1(s) + \Psi_2(s) + \Psi_3(s) \tag{19}$$

where each response in (19) represents the corresponding term in (18). The individual closed loop transfer functions in (18) are

$$F_1(s) = \frac{(\frac{fD}{HK})(\frac{I}{D}\,s + 1)}{Q(s)}\ , \tag{20}$$

$$F_2(s) = \frac{-\frac{D}{H}[\frac{HI}{KD}\,s^2 + (\frac{HD + KI}{KD})\,f_c(s)\,s + f_c(s)]}{s\,Q(s)} \tag{21}$$

and

$$F_3(s) = \frac{-(\frac{k_M D}{HK})(\frac{I}{D}\,s + 1)}{Q(s)} \tag{22}$$

where

$$Q(s) = (\frac{JI}{HK})\,s^3 + (\frac{JD + fI}{HK})\,s^2 + (\frac{fD + H^2}{HK})\,s + f_c(s)\ , \tag{23}$$

$$k = k_S k_P k_{A1} k_c k_{A2} k_M \tag{24}$$

and $f_c(s)$ is the normalized (such that $f_c(0) = 1$) open loop transfer function of the complicated compensation network. All undefined symbols here and below are defined in the list of symbols at the front of this report.

Since the system is linear, the corresponding time response $\Psi_e(t)$ is a linear combination of the time responses to the individual inputs, or

$$\Psi_e(t) = \Psi_1(t) + \Psi_2(t) + \Psi_3(t) \ , \tag{25}$$

where the terms on the righthand side of (25) represent the separate responses to the individual inputs; $\Psi_1(t)$, the response to $\dot{\Psi}_i(t)$, $\Psi_2(t)$, the response to $\dot{\Theta}_d(t)$, and $\Psi_3(t)$, the response to $e_d(t)$. As shown in [4], Appendix A-IV, each response may be expressed as the convolution of the input with the system impulse response. For the complicated transfer function involved, approximation techniques are employed below for each term.

$\Psi_1(t)$ Response to $\dot{\Psi}_i(t)$

The input $\dot{\Psi}_i(t)$ represents the vehicle angular motion about the W_i inertial axis. As shown in the diagram of Figure 5, the difference between $\dot{\Psi}_i(t)$ and the actual platform motion $\dot{\Psi}_e(t)$ is the relative motion between the vehicle and the platform which, due to the friction f in the torque motor and slip rings, causes a disturbing torque T_f to act on the platform.

For analysis a representative operational profile for vehicle angular motion about the W_i axis is assumed as illustrated in Figure 6. At launch the vehicle roll axis is coincident with the platform W_o axis so that the fluctuations about the $\dot{\Psi}_i = 0$ initially represent noise in the vehicle roll control system. At t = 5 sec. after launch, a deterministic fixed programmed roll of the vehicle is included which is quite often employed to roll the vehicle pitch plane into coincidence with the flight trajectory plane. As the vehicle rises and pitches over, the $\dot{\Psi}_i(t)$ motion about the W_i axis becomes a resolution of both pitch and yaw motion of the vehicle depending upon the pitch angle of the vehicle. The fluctuations continue throughout powered flight to time T_1 but are assumed zero during the parking orbit (i.e., the vehicle itself is stabilized with respect to the platform).

For simplicity (and a good approximation) the desired roll maneuver is represented by a fixed step Ω_1 from 5 sec. to 20 sec. and the fluctuations by a stationary process $x_1(t)$ resulting in

$$\Psi_i(t) = \begin{cases} x_1(t), & 0 < t \leq 5 \text{ sec. } ; \\ \Omega_1 + x_1(t), & 5 \text{ sec. } < t \leq 20 \text{ sec. } ; \\ x_1(t), & 20 \text{ sec. } < t \leq T_1 \ ; \\ 0, & t > T_1 \ . \end{cases} \tag{26}$$

For analysis a representative value of 2 deg./sec. is assumed for Ω_1, and $x_1(t)$ is assumed to have zero mean with a power spectral density

$$\Phi_1(\omega) = \frac{\Phi_1(0)\omega_o^2}{\omega^2 + \omega_o^2} \tag{27}$$

with $\Phi_1(0) = 0.32$ (deg./sec.)^2/(rad./sec.) and $\omega_o = 2$(rad./sec.).

Using the Nichols plot technique and nominal values for all loop parameters, the closed loop frequency response for the loop was obtained. The general type of closed loop response obtained is illustrated in Figure 7 by the $|F(j\omega)|^2$ vs. ω plot where a resonance occurs at a frequency ω_R. The frequency response of a linear system was interpreted in [4], Appendix A-VI, but for the present discussion can be considered to represent $|F_1(s)|^2_{s=j\omega}$ where $F_1(s)$ is defined by (20). For a system having a frequency response function of the type illustrated in Figure 7 with ω_R significantly large, the time response to a step input of Ω_1 magnitude is, to a close approximation, $|F(j0)|\cdot\Omega_1$.

The time response of the loop to the $x_1(t)$ input process is determined with the aid of the remaining plots in Figure 7. The center plot illustrates two continuous power spectra for the input process of the simple form assumed in (27), one with $\omega_o \ll \omega_R$ and the other with $\omega_o \gg \omega_R$. The corresponding output spectra are illustrated in the lower plot of Figure 7 which is obtained by merely multiplying the values of the top two plots. For the single-axis stabilization loop the representative value of 2 rad./sec. assumed earlier for ω_o is considerably less than ω_R for the closed loop response. The solid curve in the lower plot of Figure 7 indicates that the shape of the power spectrum is preserved. This in essence implies that $x_1(t)$ is passed through the system unchanged except for an attenuation factor

$|F(j0)|$. $|F(j0)|$ is simply the static gain of the system, or the factor fD/HK contained in (20).

The output time response $\Psi_1(t)$ to the input defined by (26) is

$$\Psi_1(t) = \begin{cases} (\frac{fD}{HK})\ x_1(t), & 0 < t \leq 5 \text{ sec. } ; \\ (\frac{fD}{HK})[\Omega_1 + x_1(t)], & 5 \text{ sec. } < t \leq 20 \text{ sec. } ; \\ (\frac{fD}{HK})\ x_1(t), & 20 \text{ sec. } < t \leq T_1 \ ; \\ 0, & t > T_1 \ . \end{cases} \tag{28}$$

$\Psi_2(t)$ Response to $\dot{\theta}_d(t)$

The input $\dot{\theta}_d(t)$ represents the residual gyro drift rate. A model based on available test data for describing the drift was developed in [5], Appendix A-IV, and is

$$\dot{\theta}_d(t) = \Delta\alpha_1 + \Delta\alpha_2 a_{SRA} + \Delta\alpha_3 a_{IA} + \beta_1 t + \beta_2 t^2 + x(t) \tag{29}$$

where $\Delta\alpha_1$ is the residual drift rate due to constant torques about the gyro OA, $\Delta\alpha_2$ and $\Delta\alpha_3$ are the residual drift rates at 1 g. acceleration due to mass unbalance along the gyro IA and SRA respectively, β_1 and β_2 represent the trend in the drift rate and x(t) is a stationary random process.

The gyro orientation with respect to the platform axes is defined in Figure 8. Assuming perfect gyro alignment in the platform,

$$a_{SRA} = a_V; \ a_{IA} = a_W \ . \tag{30}$$

Substituting the conditions of (30) into (29), the residual gyro drift rate model is stated as

$$\dot{\theta}_d(t) = \Delta\alpha_1 + \Delta\alpha_2 a_V + \Delta\alpha_3 a_W + \beta_1 t + \beta_2 t^2 + x(t) \ . \tag{31}$$

The dynamic response of the platform to gyro drift rate as defined by (18) and (19) is

$$\Psi_2(s) = F_2(s)\ \dot{\theta}_d(s) \tag{32}$$

where $F_2(s)$ is expressed by (21). First, consider a response

$$\dot{\Psi}_2(s) = s\Psi_2(s) = sF_2(s)\ \dot{\theta}_d(s) \tag{33}$$

which is the response of the platform angular rate to gyro drift rates. Multiplication of $F_2(s)$ by s in (33) cancels the extra s in the denominator of $F_2(s)$ as seen in (21). The corresponding frequency response function $|j\omega\ F_2(j\omega)|^2$ has been obtained and is similar to the $|F(j\omega)|^2$ vs. ω plot previously introduced in Figure 7. The time response $\Psi_2(t)$ can be considered by observing the frequency response to each individual term in $\dot{\theta}_d$.

In the discussion in [5], Appendix A-IV of the gyro drift rate model to be used in analysis the first term $\Delta\alpha_1$ was recognized as a random variable, constant over time. The time response of the platform angular rate to the constant $\Delta\alpha_1$ input simply results by multiplying $\Delta\alpha_1$ by the static gain -D/H.

In the second and third terms of $\dot{\theta}_d$, $\Delta\alpha_2$ and $\Delta\alpha_3$ are also random variables, but the response to these input terms is dependent upon the frequency content of the accelerations a_V and a_W. Gyro tests were conducted under 1 g. (32.2 ft./sec.^{2}) acceleration due to gravity to measure $\Delta\alpha_2$ and $\Delta\alpha_3$. No tests were observed conducted whereby the gyro drift behavior was measured under vibratory acceleration conditions. Since this effect is unknown, the gyro drift rate model is restricted to linear accelerations by assuming a linear extrapolation of the acceleration-sensitive drift rates from 1 g. to other acceleration levels. For analysis the required linear accelerations are defined by the nominal acceleration profile for the mission. Typical acceleration profiles for actual vehicle boost phases are illustrated by the dashed curves in Figure 9. Since the functions are slowly varying (containing primarily low frequency components only), it is sufficient for analysis to approximate these profiles by the solid curves in Figure where the approximation maintains the magnitudes of the accelerations in the typical profiles. Thus

$$a_V = A_1 t \ ; \ A_1 = \frac{110 \ (\text{ft./sec.}^2)}{230 \ (\text{sec.})} \tag{34}$$

and

$$a_W = B_o + B_1 t \ ; \ B_o = 110 \ (\text{ft./sec.}^2) \ , \ B_1 = \frac{220 \ (\text{ft./sec.}^2)}{230 \ (\text{sec.})} \ . \tag{35}$$

Because of the slow variations in a_V and a_W, the time response of the platform angular rate is sufficiently represented by multiplication of each term by the static gain -D/H.

The β_1 and β_2 coefficients in the fourth and fifth term of $\dot{\theta}_d$ are also random variables. As observed from actual gyro data, the range of values of β_1 and β_2 are sufficiently small so that the terms containing these variables may also be considered slowly-varying quantities with the time response of the platform angular rate obtained by multiplying the terms by the static gain -D/H.

The latter term x(t) is described in [5], Appendix A-III as a stationary random process with zero mean. In [7] two possible models based on actual data are presented for describing x(t). Model I assumes the process to represent essentially band-limited "white" noise described by the power spectral density

$$\Phi_I(\omega) = \begin{cases} \Phi_I(0), & 0 \leq |\omega| \leq \omega_1 \\ 0, & |\omega| > \omega_1 \ . \end{cases} \tag{36}$$

Model II assumes a process resulting from passing "white" noise through a linear filter possessing a bandpass equivalent to the gyro bandwidth yielding a power spectral density

$$\Phi_{II}(\omega) = \frac{\Phi_{II}(0)\omega_g^2}{\omega^2 + \omega_g^2} \tag{37}$$

where ω_g is the gyro bandpass frequency. ω_1 is considerably less than ω_g, and it is known that the gyro drift rate trace from which the power spectrum in Model I was estimated did not contain the higher frequencies due to a low

bandpass of the recording device. Therefore, Model II is physically more appealing in that it contains the higher frequencies actually passed by the gyro.

The time response of the platform angular rate to the x(t) input yields an output process $x_2(t)$ which is determined by the system bandpass characteristics defined by $|(j\omega)\ F_2(j\omega)|^2$. Assuming the Model II for x(t), the power spectral density characterized by (37) is illustrated by the dashed curve in the center plot of Figure 7 to show its relationship to the system bandpass characteristics. The dashed curve in the lower plot of Figure 7 illustrates the filtering or attenuation of the higher frequencies above the system bandpass. The power spectral density of the output process $x_2(t)$ is expressed by

$$\Phi_2(\omega) = |(j\omega)\ F_2(j\omega)|^2 \Phi_{II}(\omega) \ . \tag{38}$$

To prevent laborious calculations, a close approximation to $\Phi_2(\omega)$ is obtained by recognizing the sharp cut-off of the system frequency bandpass. It is evident that $\Phi_2(\omega)$ is closely approximated by

$$\Phi_2(\omega) = \begin{cases} (\frac{D}{H})^2\ \Phi_{II}(0), & 0 \leq |\omega| \leq \omega_s \\ 0, & |\omega| > \omega_s \ , \end{cases} \tag{39}$$

where ω_s is the effective bandpass frequency of the system, D/H is the magnitude of the system static gain and $\Phi_{II}(0)$ is defined in (37).

The time response $\dot{\Psi}_2(t)$ of the platform angular rate to gyro drift rates has been discussed term by term. Collecting all the responses into a single expression yields

$$\dot{\Psi}_2(t) = -\frac{D}{H}[\Delta\alpha_1 + \Delta\alpha_2 A_1 t + \Delta\alpha_3 B_0 + \Delta\alpha_3 B_1 t + \beta_1 t + \beta_2 t^2] + x_2(t) \ . \tag{40}$$

Prime interest in the analysis is on the time response $\Psi_2(t)$ representing the time behavior of the platform angle. The dynamic response of the platform angle is

$$\Psi_2(s) = \frac{1}{s}\,\dot{\Psi}_2(s) = F_2(s)\,\dot{\theta}_d(s)\ , \tag{41}$$

and in [4], Appendix A-II, it is shown that division by s in the complex s domain is equivalent to integration over time in the time domain. Therefore, the time response of the platform angle is

$$\Psi_2(t) = \begin{cases} -\frac{D}{H}\left[\Delta\alpha_1 t + \frac{\Delta\alpha_2 A_1 t^2}{2} + \Delta\alpha_3\left(B_o t + \frac{B_1 t^2}{2}\right) + \frac{\beta_1 t^2}{2} + \frac{\beta_2 t^3}{3}\right] + \int_o^t x_2(\tau)\,d\tau\ , & 0 < t \le T_1 \\ -\frac{D}{H}\left[\Delta\alpha_1 t + \frac{\Delta\alpha_2 A_1 T_1^2}{2} + \Delta\alpha_3\left(B_o T_1 + \frac{B_1 T_1^2}{2}\right) + \frac{\beta_1 t^2}{2} + \frac{\beta_2 t^3}{3}\right] + \int_o^t x_2(\tau)\,d\tau\ , & T_1 < t \le T_2\ . \end{cases} \tag{42}$$

$\Psi_3(t)$ Response to $e_d(t)$

The input $e_d(t)$ represents the GCA (gimbal control amplifier) output null current. As reported in [5], no measurements were observed which yielded data reflecting the behavior of $e_d(t)$ over time.

To simply illustrate that this effect can be considered in the reliability analysis, a GCA output bias is assumed present. For purposes of demonstration $e_d(t)$ is considered to be represented by linear drift

$$e_d(t) = \gamma_o + \gamma_1 t\ , \tag{43}$$

where the coefficients γ_o and γ_1 are random variables with both having relatively small standard deviations.

The dynamic response of the system to the GCA output bias as defined by (18) and (19) is

$$\Psi_3(s) = F_3(s)\,e_d(s)\ , \tag{44}$$

where $F_3(s)$ is more explicitly defined in (22). The frequency response function $|F_3(j\omega)|^2$ is again similar to the $|F(j\omega)|^2$ vs. ω plot illustrated in Figure 7 with the static gain $|F(jo)| = -k_M D/HK$.

Since γ_1 in (43) is considered small, $e_d(t)$ is also a slowly-varying function of time. Therefore, the corresponding time response $\Psi_3(t)$ of the platform angle to the GCA output bias is sufficiently represented by mere multiplication of $e_d(t)$ by the static gain yielding

$$\Psi_3(t) = -K_3[\gamma_o + \gamma_1 t] \ , \tag{45}$$

where

$$K_3 = \frac{k_M D}{HK} \ .$$

Total Loop Time Response, $\Psi_e(t)$

The total time response $\Psi_e(t)$ of the platform angle is expressed by (25) as the linear combination of the individual responses obtained above. The attributes required to predict the reliability of the loop are identified in (16) and (17) as $V_U(T_1)$ and $\Psi_e(T_2)$.

$V_U(T_1)$ is obtained by first substituting (28), (42) and (45) into (25), then substituting the result into the integrand of (10) and performing the indicated integration from 0 to T_1 with $a_V = A_1 t$. This results in

$$\begin{aligned} V_U(T_1) = A_1\{- \frac{fD}{HK}[\frac{375K_1}{2} &+ \int_o^{T_1} t\, x_1(t)\, dt] \\ &+ \frac{D}{H}[\frac{T_1^3\, \Delta\alpha_1}{3} \quad \frac{A_1 T_1^4\, \Delta\alpha_2}{8} + (\frac{B_o T_1^3}{3} + \frac{B_1 T_1^4}{8})\, \Delta\alpha_3 \\ &+ \frac{T_1^4 \beta_1}{8} \quad \frac{T_1^5 \beta_2}{15}] + \int_o^{T_1} t \int_o^{t} x_2(\tau)\, d\tau dt \\ &+ K_3[\frac{T_1^2}{2}\gamma_o + \frac{T_1^3}{3}\gamma_1]\} \end{aligned} \tag{46}$$

$\Psi_e(T_2)$ is obtained by substituting (28), (42) and (45) into (25) and setting $t = T_2$ which yields

$$\begin{aligned} \Psi_e(T_2) = - \frac{D}{H}[T_2\, \Delta\alpha_1 &+ \frac{A_1 T_1^2}{2}\Delta\alpha_2 + (B_o T_1 + \frac{B_1 T_1^2}{2})\, \Delta\alpha_3 \\ &+ \frac{T_2^2}{2}\beta_1 + \frac{T_2^3}{3}\beta_2] + \int_o^{T_2} x_2(\tau)\, d\tau \\ &+ K_3[\gamma_o + T_2\gamma_1] \ . \end{aligned} \tag{47}$$

VI. Statistical Analysis

A. Data Used in the Statistical Analysis

Three types of data secured from MH were used in the statistical analysis. All three were associated with the gyro. They were measurements of the drift variables CT, MUIA, and MUSRA, a continuous strip chart recording of random gyro drift rate over a three hour period, and six-minute averages calculated from a number of such continuous recordings.

The measurements of the drift variables are exemplified by Figure 10, where the data plotted represent measurements of either CT, MUIA, or MUSRA. The horizontal scale is in degrees/hr. for CT or degrees/hr./g for MUIA or MUSRA. The vertical scale indicates test conditions in both Minneapolis and Florida, with the chronological order in the down direction.

There were five such charts, three of which carried plots for MUIA and MUSRA, one had plots for MUIA, MUSRA, and CT, and one had plots for MUIA and MUSRA, with numbers recorded for CT. Thus, there were five sets of data for MUIA and MUSRA, but only two sets for CT.

A continuous strip chart recording was obtained for only a single gyro, and was used in the analysis to illustrate how to analyze the purely stochastic component of the drift. The strip chart contained two three-hour traces of random drift rate for the gyro, one with the output axis in the vertical position (OAV) and the other with the output axis in the horizontal position (OAH), as described in [5], Appendix A-III. Because the second recording measures the sum of g-sensitive and g-insensitive drift rates in such a way that they cannot be separated, it was not used in the analysis. The first recording, which measures only the g-insensitive rate, was used.

Thirty averages over successive six-minute periods were obtained from the three-hour OAV traces for twenty-two gyros, including the strip chart recording discussed above. The six-minute averages were obtained either manually or with an integrator. In neither case was the absolute gyro drift rate determined from the available information. However, using the strip chart recordings, an appropriate origin and scale were devised which would simulate real drift rates. A typical set of averages, together with a fitted curve which is described in the sequel, is plotted in Figure 11.

Of the five gyros for which drift variable measurements were secured, only one occurred in the set of twenty-two, and this was not the gyro with the strip chart recording. Accordingly, the complete analysis cannot be carried out separately for each individual gyro, although in practice it may normally be desirable to do so.

In order to make the analysis more realistic, it was desired to introduce the effects of frictional torques of the slip rings and torque motors which act as disturbing torques on the gimbal. The effects of viscous frictional torques resulting from vehicle angular motion were defined by (28) in which both deterministic and random motion were considered. At the low viscous friction levels encountered, the loop degradation due to the deterministic motion assumed has been computed and shown to be insignificant in comparison to the random component. To include the effects of Coulomb and break-away frictional torques for the slip rings and torque motor, sample data sheets were drawn and the torques recorded. However, as was indicated earlier, the attempt to simulate the loop with the non-linear effects present did not succeed, and hence it was not possible to utilize the torque measurements. Because they were not used in the analysis, no typical data are included herein.

Finally, in order to include some element other than the gyro in the analysis of the loop, even though no suitable data were available, it was decided to introduce synthetic data. This was done by defining e_d, the GCA null current, to be a linear function of time as defined in (43). It is supposed in the following analysis that the coefficient γ_1 is so small that it may be neglected. However, γ_o will be assumed a random variable with zero mean and standard deviation .00567 amp., and will be included in the analysis.

B. <u>General Method of Reliability Estimation</u>

It is required to estimate the probabilities of the events

$$\{|V_U(T_1)| \leq V_U'\} , \tag{48}$$

$$\{|\Psi_e(T_2)| \leq \Psi_e'\} , \tag{49}$$

and the joint event, (48) and (49). To do so would require data obtained under actual or simulated mission conditions. Because such data were not available, the above probabilities will be estimated using data obtained under manufacturing conditions, as was discussed in connection with (16) and (17).

If the form of the bivariate distribution of $V_U(T_1)$ and $\Psi_e(T_2)$ is known, and if data are available for estimating the parameters of the distribution, then both the probability density function and the required probabilities may be estimated. The probabilities also may be estimated when the form of the bivariate and univariate distributions are not known, but such estimates are generally much less precise.

In the present instance, there is strong reason to believe that the bivariate distribution is approximately bivariate normal with zero means. Because both $V_U(T_1)$ and $\Psi_e(T_2)$ are linear functions of several random variables which presumably are not highly correlated, it follows from the Central Limit Theorem that they are approximately normally distributed. Furthermore, some of the individual random variables appear to be approximately normally distributed.

The random variables which are common to the two functions are $\Delta\alpha_1$, $\Delta\alpha_2$, $\Delta\alpha_3$, β_1, β_2, and e_d. In addition, the random variables $\int_0^{T_1} t\, x_1(t)\, dt$ and $\int_0^{T_1} t \int_0^t x_2(\tau)\, d\tau dt$ occur in $V_U(T_1)$. Clearly, the expected value of all nine of these random variables is zero, and, hence, so are the expected values of $V_U(T_1)$ and $\Psi_e(T_2)$.

Although normality of the marginal distributions does not imply that the bivariate distribution is normal, still it is reasonable to assume that it is. The approach to be followed, then, is to estimate the variances of $V_U(T_1)$ and $\Psi_e(T_2)$ and their covariance, and thence, using normal theory, the required probabilities.

The variances of $V_U(T_1)$, $\Psi_e(T_2)$, and their covariance, as computed from (46) and (47) are given below. Most of the covariance terms have been omitted because they are thought to be zero for reasons which will be presented in later discussion.

$$\mathrm{Var}(V_U(T_1)) = (-A_1 \frac{fD}{HK})^2 \mathrm{Var}(\int_o^{T_1} t\, x_1(t)\, dt)$$

$$+ (\frac{D}{H} A_1)^2 [T_1^3/3)^2 \mathrm{Var}(\Delta\alpha_1) + (A_1 T_1^4/8)^2 \mathrm{Var}(\Delta\alpha_2)$$

$$+ (B_o T_1^3/3 + B_1 T_1^4/8)^2 \mathrm{Var}(\Delta\alpha_3)$$

$$+ (T_1^4/8)^2 \mathrm{Var}(\beta_1) + T_1^5/15)^2 \mathrm{Var}(\beta_2)$$

$$+ 2(T_1^4/8)(T_1^5/15) \mathrm{Cov}(\beta_1,\beta_2) + \mathrm{Var}(\int_o^{T_1} t \int_o^t x(\tau)\, d\tau dt)]$$

$$+ (K_3 A_1 T_1^2/2)^2 \mathrm{Var}(\gamma_o) \qquad (50)$$

$$\mathrm{Var}(\Psi_e(T_2)) = (-\frac{D}{H})^2 [T_2^2 \mathrm{Var}(\Delta\alpha_1) + (A_1 T_1^2/2)^2 \mathrm{Var}(\Delta\alpha_2)$$

$$+ (B_o T_1 + B_1 T_1^2/2)^2 \mathrm{Var}(\Delta\alpha_3) + (T_2^2/2)^2 \mathrm{Var}\ \beta_1$$

$$+ (T_2^3/3)^2 \mathrm{Var}\ \beta_2 + (T_2^5/3) \mathrm{Cov}(\beta_1,\beta_2)$$

$$+ \mathrm{Var}(\int_o^{T_2} x(\tau)\, d\tau)] + (-K_3)^2 \mathrm{Var}(\gamma_o) \qquad (51)$$

$$\mathrm{Cov}(\Psi_e, V_U) = (\frac{D}{H})^2 A_1 T_1^3 [(T_2/3) \mathrm{Var}(\Delta\alpha_1) + (A_1^2 T_1^3/16) \mathrm{Var}(\Delta\alpha_2)$$

$$+ (B_o T_1 + B_1 T_1^2/2)(B_o/3 + B_1 T_1/8) \mathrm{Var}(\Delta\alpha_3)$$

$$+ (T_1 T_2^2/16) \mathrm{Var}\ \beta_1 + (T_1^2 T_2^3/45) \mathrm{Var}\ \beta_2$$

$$+ (T_1^2 T_2^2/30 + T_1 T_2^3/24) \mathrm{Cov}(\beta_1,\beta_2)$$

$$+ \mathrm{Cov}(\int_o^{T_2} x(\tau)\, d\tau, \int_o^{T_1} t \int_o^t x(\tau)\, d\tau dt]$$

$$+ (-K_3)^2 A_1 T_1^2/2) \mathrm{Var}(\gamma_o) \qquad (52)$$

C. Variances of Drift Variables

The drift variables α_1, α_2, and α_3 are measured in the hangar just prior to transferring the system to the launch pad, and compensating corrections are programmed into the computer, as discussed in [5], Appendix A-IV. The quantities $\Delta\alpha_1$, $\Delta\alpha_2$, and $\Delta\alpha_3$ are changes which occur in α_1, α_2, and α_3 during the transfer to the pad and therefore are residual drifts which are not compensated for.

If α_1, α_2, and α_3 could be measured while the system was on the launch pad and their observed values used for drift compensation, then $\Delta\alpha_1$, $\Delta\alpha_2$, and $\Delta\alpha_3$ would represent only measurement error. However, no such measurements were available for the present analysis, and could not ever be available for a given system until it is built and moved to the launch site. Even then, if it were impossible to measure α_1, α_2, and α_3 on the pad, $\Delta\alpha_1$, $\Delta\alpha_2$, and $\Delta\alpha_3$ could be estimated by simulating the hangar to pad sequence, making both sets of measurements in the hangar or elsewhere where suitable measurements could be made. It would be possible, of course, to use such measurements from previous similar systems, if available.

In the present instance, production test data were used to estimate $\Delta\alpha_1$, $\Delta\alpha_2$, and $\Delta\alpha_3$. A typical set of such data for a single gyro was introduced in Figure 10. A set of measurements like those may be regarded as a sample from a population of similar measurements which conceptually could be made on the gyro. From this point of view, the variance calculated from the measurements, the sample variance, is an estimate of the unknown population variance. In particular, it estimates the variance of the shift in the drift variable from the hangar to the pad. A caret (^) over a symbol will indicate a sample estimate of a population parameter.

For each of five gyros, the sample variance was computed for α_2 and α_3, and for two gyros, for α_1. A typical calculation, which is explained further in the next paragraph, is shown in Table I. The several variances for each drift variable were averaged to obtain a typical variance, which was used in the subsequent analysis. These are shown in Table II. Of course, in normal practice, the correct variances would be the variances associated with the gyro in the loop, not averages over several gyros.

There are some qualifications to the simple procedure just described. Perusal of Figure 10 suggests that there are certain groups of tests carried out under nearly similar conditions. For example, in Florida there were sets of post-cool measurements which seem to constitute groups of two and three measurements. Such groups have been distinguished in Table I. An analysis of variance was carried out by introducing a within-group variance and a between-group variance, and the sum of the variances was estimated. The within-group variances usually were small compared to the between-group variances. Moreover, the expectation of the total sample variance, i.e., the sample variance without grouping, already discussed above, was very close to the sum of the within-group and between-group variances. Although the latter sum was used in the present analysis, it differed very little from the total sample variance.

Also, there may be serial correlation between successive measurements. If so, the sample variance is not an appropriate estimate of the variance of the shift in the drift variable from the hangar to the pad. Another point to be considered is whether or not the differences among test conditions, such as vibration versus non-vibration and severe temperatures versus normal operating temperatures, adequately simulate the change in conditions between the hangar and the pad.

The existence or non-existence of correlation between $\Delta\alpha_1$, $\Delta\alpha_2$, and $\Delta\alpha_3$ was examined by constructing plots of $\Delta\alpha_1$ versus $\Delta\alpha_2$, $\Delta\alpha_1$ versus $\Delta\alpha_3$, and $\Delta\alpha_2$ versus $\Delta\alpha_3$. The data were so sparse that no decision could be reached, but it did appear that correlation, if present, was small. Accordingly, the analysis was carried out by assuming no correlation among the $\Delta\alpha$'s. A typical plot is shown in Figure 12.

D. Variances of Time Trend Variables

It is likely that the trend in the drift rate differs among gyros. If so, then each gyro has its own characteristic β_1 and β_2, which should be estimated from observing the drift rate over time for that gyro. A single set of averages, such as those available from the three hour strip chart recording, would provide one observation on the pair (β_1, β_2). This would not be a precise estimate of (β_1, β_2) and would not permit estimates of the variances of β_1 and β_2 or of their covariance. Accordingly, a number of runs would be required.

Because only one drift run was available for each gyro, it was decided for the present analysis that the data for different gyros would be used to estimate the variances of β_1 and β_2 and their covariance. This is a reasonable thing to do if the variation among drift runs from gyro to gyro is of about the same order of magnitude as the variation among repeated drift runs for the same gyro. The analysis is described in the sequel.

There were thirty six-minute averages for each of twenty-two gyros. The following analysis was applied to all but one gyro, which was omitted because it exhibited unusually large variability. The quadratic function $y = \alpha_1 + \beta_1 t + \beta_2 t^2$ was fitted to each set of averages by the method of least squares. In this equation, y is the drift rate in degrees per hour, α_1 is the drift rate due to constant torque, and β_1 and β_2 are coefficients of powers of t. For one gyro, the first four averages were omitted because it appeared that the test conditions had not yet stabilized. The twenty-one estimates of β_1 and β_2 are shown in Table III. Also shown are the estimated variances of $\hat{\beta}_1$, which will be referred to below as within gyro estimates.

Attention was given to serial correlation among the averages, and it was found that the serial correlation among successive averages was about .45. Although the method of least squares as it was used assumes independent observations, it still is highly efficient in the presence of such low serial correlation.

The variances of $\hat{\beta}_1$ and $\hat{\beta}_2$ and their covariance were estimated from the twenty-one sets of $(\hat{\beta}_1, \hat{\beta}_2)$. The calculation is shown in Table IV. It should be noted that the variance among the $\hat{\beta}_1$'s estimates the sum of the between gyro component of variance and the within gyro component. The latter was estimated by averaging the twenty-one within gyro estimates of variance, and then it was subtracted out to leave an estimate of the between gyro component of variance. Similar calculations were carried out to estimate the variance of β_2 and the covariance of β_1 and β_2.

E. Variances of Random Process and Associated Random Variables

The residual variation around the trend in a strip chart recording has been denoted by $x_2(t)$, which is a non-deterministic random process. The quantities $\int_0^{T_1} t \int_0^t x_2(\tau)\, d\tau$ in $V_U(T_1)$ and $\int_0^{T_2} x_2(\tau)\, d\tau$ in $\Psi_e(T_2)$ are random

variables, and it is desired to determine their variances and covariance. The variance of the first variable and the covariance of both have not been evaluated for this analysis, although, in principle, it can be done. The formulae are well-known and would, in practice, be evaluated by an electronic computer. Failure to do so herein does not materially affect the further analysis, because it is evident that the variances and covariance are small in comparison to other variances in $\Psi_e(T_2)$ and $V_U(T_1)$.

For evaluating the variance of the second variable, only one strip chart recording of the random gyro drift rate process was available, and fifty minutes of it was used for analysis. An analysis which was conducted and reported in [7] was principally concerned with the original gyro drift rate process x(t) and with measures of performance other than the variance. On page two of that report the observed sample variance of x(t) is given, and Figure 7 of that report is a plot of the variance of $\int_0^T x(\tau)\, d\tau$ in degrees against time T in hours. This was calculated under Model II of the report. As discussed in connection with (42), the variable $\int_0^{T_2} x_2(\tau)\, d\tau$ results from x(t) being passed through the assumed linear system, and its variance has been evaluated and listed in Table V.

Other covariances could not be estimated from the data in the form in which it was available. It is conceivable, e.g., that non-zero covariances could exist between the $\Delta\alpha$'s and the β's. But in order to estimate such covariances, it would be necessary to observe the $\Delta\alpha$'s and the β's at the same time, so that they would be grouped, and to have several such observations made at different times.

Substitution of the estimated variances and covariances into formulae (50), (51), and (52) yields $\mathrm{Var}(V_U(T_1))$, $\mathrm{Var}(\Psi_e(T_2))$, and $\mathrm{Cov}(V_U(T_1),\Psi_e(T_2))$, which are shown in Table V. Also presented is the estimated correlation coefficient $\hat{\rho}(\Psi_e,V_U)$.

F. Estimation of Reliability

There is good reason to believe that the variables $V_U(T_1)$ and $\Psi_e(T_2)$ are approximately normally distributed. This follows from the consideration that each of them is a linear function of several statistically independent, or at least presumably not highly correlated, random variables. Furthermore,

for some of the variables there is evidence that they themselves are approximately normally distributed. This is true for β_1 and β_2, as is indicated by plots on normal probability paper, shown in Figure 13. In addition, for the process $x_2(t)$, it was found in [7] that the assumption of a Gaussian process is compatible with the data, and hence the integral $\int_0^t x_2(\tau)\, d\tau$ should be approximately Gaussian.

Assuming that $V_U(T_1)$ and $\Psi_e(T_2)$ are normally distributed, the probabilities of the events (48) and (49) may be calculated. This has been done by employing the standard deviations of V_U and Ψ_e to look up areas under the normal curve. These areas have been used to plot the center lines on Figures 14 and 15, which show how the probabilities vary with the allowable errors in velocity and drift. The probability of event (48) is the reliability at time T_1 and has been so labeled on Figure 14.

The simple procedure just described results in biased estimates of the reliabilities. However, if the numbers of degrees of freedom associated with the estimates of the variances are sufficiently large, the biases are negligible. In the present instance, such is the case. If unbiased estimates are desired, they may be found by the procedure described in [9]. To calculate confidence intervals requires the use of the theory of tolerance intervals, as described in [10]. This has been applied and the limits are shown on Figures 14 and 15.

To estimate the reliability at time T_2 it is necessary to estimate the probability of the joint event (48) and (49). This can be done most correctly by use of the appropriate bivariate distribution. Although data are not available to support or refute the conjecture that the distribution is bivariate normal, it seems quite reasonable to assume that it is. However, in view of the small value of $\hat{\rho}(V_U, \Psi_e)$, the variables may, without much bias in estimation, be treated as statistically independent. To do so implies that the desired probabilities may be estimated by multiplying together the appropriate separate probabilities.

VII. Acknowledgment

The authors wish to express their appreciation to the Minneapolis-Honeywell Regulator Company for giving them ready access to its facility in St. Petersburg, Florida, and for the cooperation and assistance rendered by

its personnel. Particular thanks are due to Mr. Marion Smith and his staff.

The authors also wish to express their appreciation to Dr. David Gaylor of the Institute for his contributions to the statistical analysis, which included carrying out the analysis discussed in VI-D and consultation on other aspects of the work.

REFERENCES

1. Lewis, J. B. and Wells, W. T., "Probabilistic Models for Predicting System Reliability," Working Paper No. 3, September, 1962, Contract NASw-334, Research Triangle Institute, Durham, North Carolina.

2. Thompson, W. S., "Probabilistic Models for Predicting System Reliability-Application to CENTAUR Inertial Guidance System," Working Paper No. 4, December, 1962, Contract NASw-334, Research Triangle Institute, Durham, North Carolina.

3. Thompson, W. S., "Data for the Reliability Analysis of the CENTAUR Azimuth Gimbal Stabilization Loop," Working Paper No. 6 (CONFIDENTIAL), January, 1963, Contract NASw-334, Research Triangle Institute, Durham, North Carolina.

4. Thompson, W. S., "Functional Description of a Single-axis Stabilization Loop of a Stable Platform," Working Paper No. 8, August, 1963, Contract NASw-334, Research Triangle Institute, Durham, North Carolina.

5. Connor, W. S. and Thompson, W. S., "An Appraisal for Use in Reliability Analysis of the Test and Data Collection Procedures in the Manufacture of an Inertial Guidance System," Working Paper No. 10, November, 1963, Contract NASw-334, Research Triangle Institute, Durham, North Carolina.

6. Fernandez, M. and Macomber, G. R., Inertial Guidance Engineering, Chapter 3, Prentice-Hall, Inc., 1962.

7. Cryer, J. D. and Leadbetter, M. R., "Analysis of Random Gyro Drift-rate Data," Working Paper No. 9, August, 1963, Contract NASw-334, Research Triangle Institute, Durham, North Carolina. (CONFIDENTIAL)

8. Connor, W. S. and Thompson, W. S., "Tables to Accompany Reliability Analysis of the CENTAUR IGS First Gimbal Stabilization Loop," Working Paper No. 11, December, 1963, Contract NASw-334, Research Triangle Institute, Durham, North Carolina.

9. Bowker, Albert H. and Lieberman, Gerald J., Engineering Statistics, Prentice-Hall, Inc., 1959, pp. 470 ff.

10. Proschan, Frank, "Confidence and Tolerance Intervals for the Normal Distribution," Journal of the American Statistical Association, Vol. 48, 1953, pp. 550-564.

Table I[1]

ESTIMATION OF THE VARIANCE OF MUSRA, (α_3), FOR A PARTICULAR GYRO

(Values of MUSRA in Deg./Hr./g)

Group	MUSRA	Group	MUSRA	Group	MUSRA
1		6		9	
2		7		10	
3		7		10	
4		7		11	
3		8		12	
5		9		13	

ANALYSIS OF VARIANCE

Source of Variation	Degrees of Freedom	Sum of Squares	Mean Square	Expected Mean Square
Between Groups	12			$\sigma_w^2 + 1.36\ \sigma_b^2$
Within Groups	5			σ_w^2
Total	17			$\sigma_w^2 + .96\ \sigma_b^2$

$\hat{\sigma}_b^2 =$ and $\hat{\sigma}_b^2 + \hat{\sigma}_w^2 =$, where σ_w^2 is the within-group variance, and σ_b^2 is the between-group variance.

[1]The data have been omitted from these tables in order to avoid the necessity of classifying this report. The completed tables appear in a separate classified report, Reference 8 in the list of references.

Table II[1]

ESTIMATED VARIANCES OF CT, MUIA, AND MUSRA
FOR ALL GYROS

[CT is in $(0/Hr.)^2$ and MUIA and MUSRA are in $(0/Hr./g)^2$]

Gyro	CT	MUIA	MUSRA
	(α_1)	(α_2)	(α_3)
1			
2			
3			
4			
5			
Average			

[1]The data have been omitted from these tables in order to avoid the necessity of classifying this report. The completed tables appear in a separate classified report, Reference 8 in the list of references.

Table III[1]

Estimates of β_1 and β_2 and Associated Variances

Gyro	$\hat{\beta}_1$	$\hat{\beta}_2$	$Var(\hat{\beta}_1)$
1			
2			
3			
4			
5			
6			
7			
8			
9			
10			
11			
12			
13			
14			
15			
16			
17			
18			
19			
20			
21			
		Average	

[1]The data have been omitted from these tables in order to avoid the necessity of classifying this report. The completed tables appear in a separate classified report, Reference 8 in the list of references.

Table IV[1]

ESTIMATION OF THE BETWEEN GYROS
COMPONENT OF VARIANCE OF β_1

Sums of Squares:

$\Sigma \hat{\beta}_1^2 =$

$(\Sigma \hat{\beta}_1)^2/21 =$

Mean Square:

Within Gyros
(from Table III):

[1]The data have been omitted from these tables in order to avoid the necessity of classifying this report. The completed tables appear in a separate classified report, Reference 8 in the list of references.

Table V[1]

ESTIMATED VARIANCES, COVARIANCES AND CORRELATION

Quantity	Variance	Units
$\Delta\alpha_1$		$(\text{rad/sec})^2$
$\Delta\alpha_2$		$[(\text{rad/sec})/(\text{ft/sec}^2)]^2$
$\Delta\alpha_3$		$[(\text{rad/sec})/(\text{ft/sec}^2)]^2$
β_1		$[(\text{rad/sec}^2)]^2$
β_2		$[(\text{rad/sec}^3)]^2$
γ_o		$(\text{amp})^2$
$\int_o^{T_2} x_2(t)\, dt$		$(\text{rad})^2$
$\int_o^{T_1} t\, x_1(t)\, dt$		$(\text{sec})^2$
$V_U(T_1)$		$(\text{ft/sec})^2$
$\Psi_e(T_2)$		$(\text{rad})^2$
$\hat{\text{Cov}}(\beta_1,\beta_2)$		$(\text{ft}^2/\text{sec}^5)$
$\hat{\text{Cov}}(V_U(T_1), \Psi_e(T_2))$		(rad.ft/sec)
$\hat{\rho}(V_U,\Psi_e)$		

[1]The data have been omitted from these tables in order to avoid the necessity of classifying this report. The completed tables appear in a separate classified report, Reference 8 in the list of references.

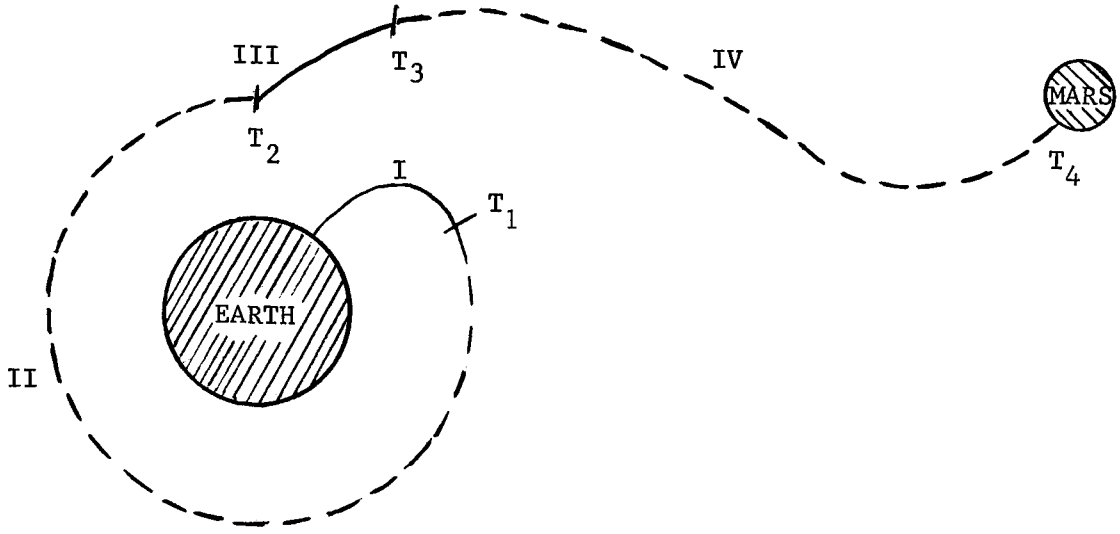

Figure 1. Simplified Description of Vehicle Mission

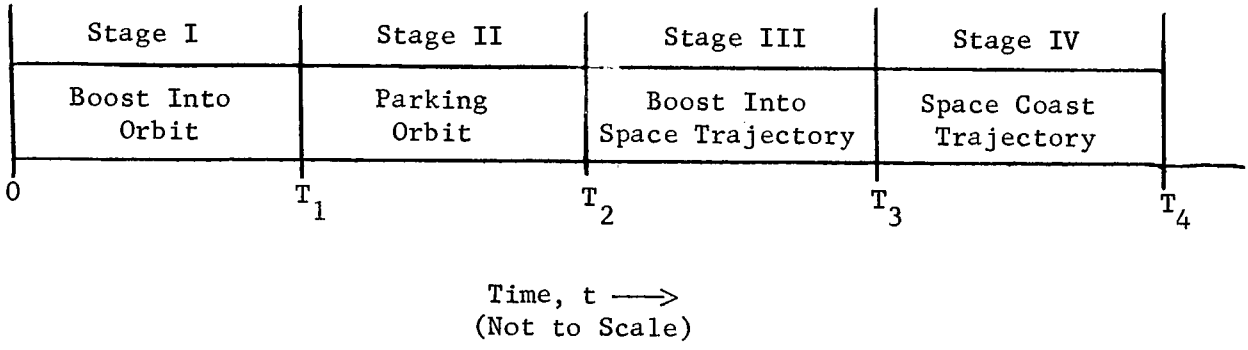

Figure 2. Major Sequential Stages of System Operation

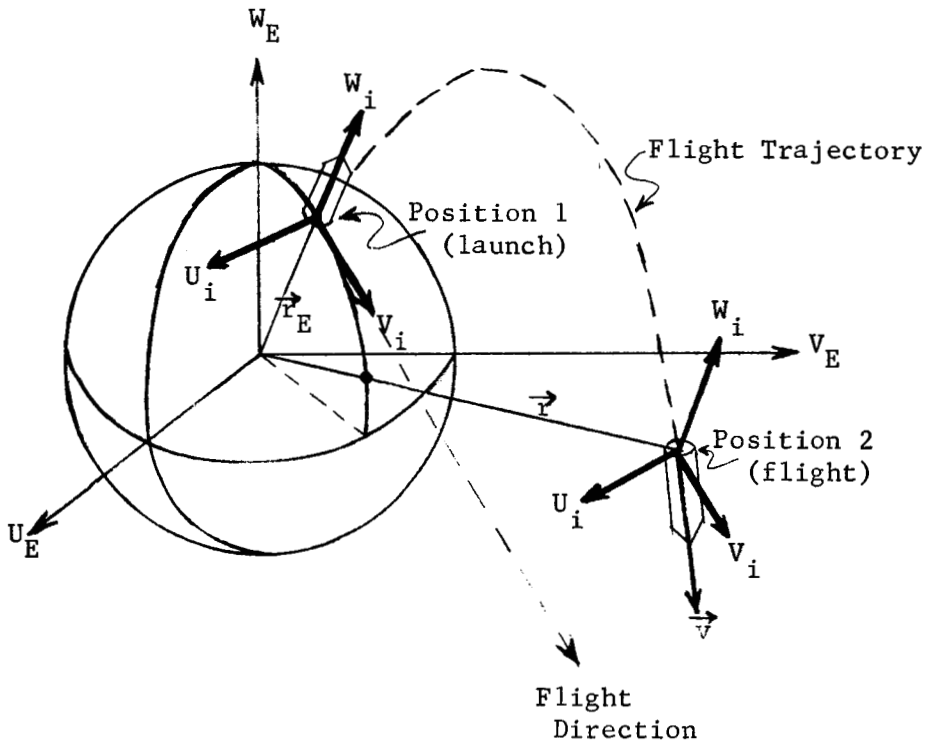

Figure 3. Geometry for an Ideal Stable Platform

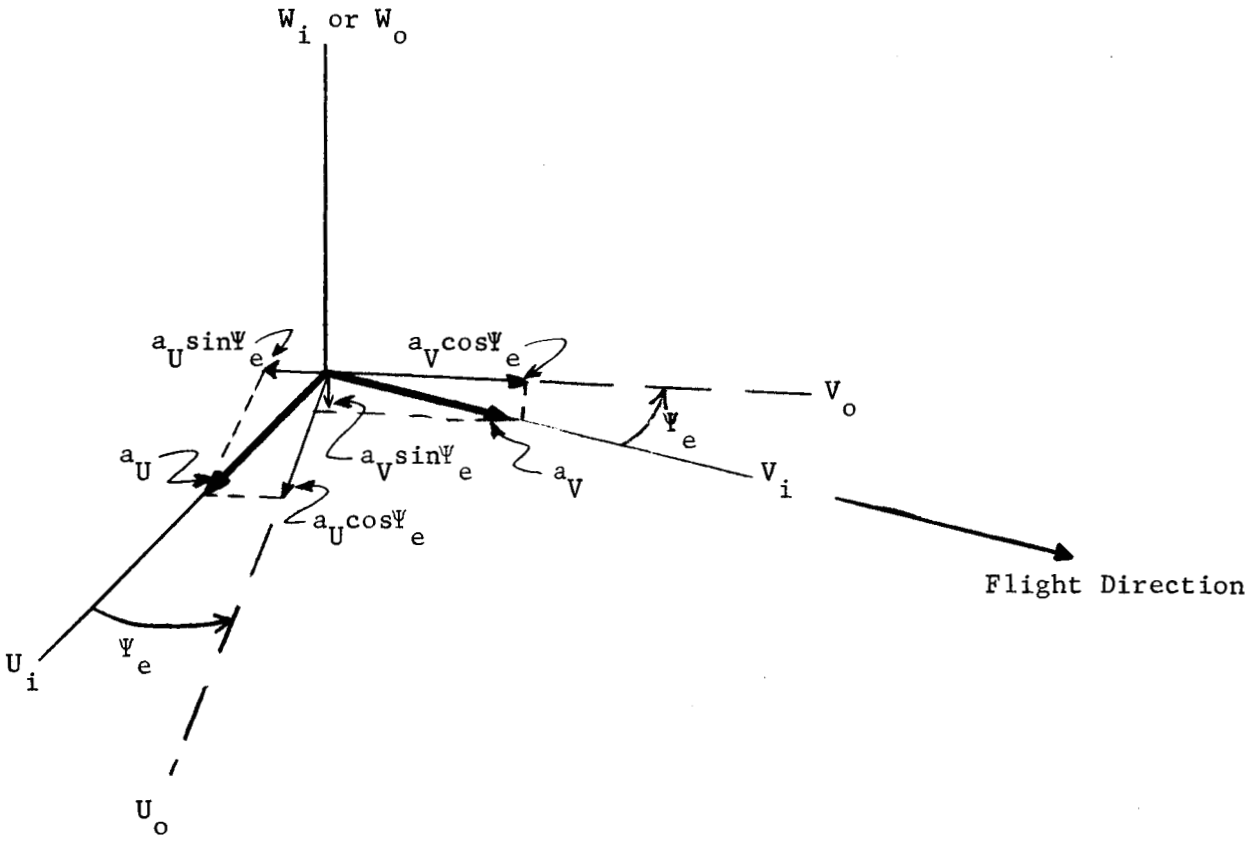

Figure 4. Effect of Platform Azimuth Drift on Measured Accelerations

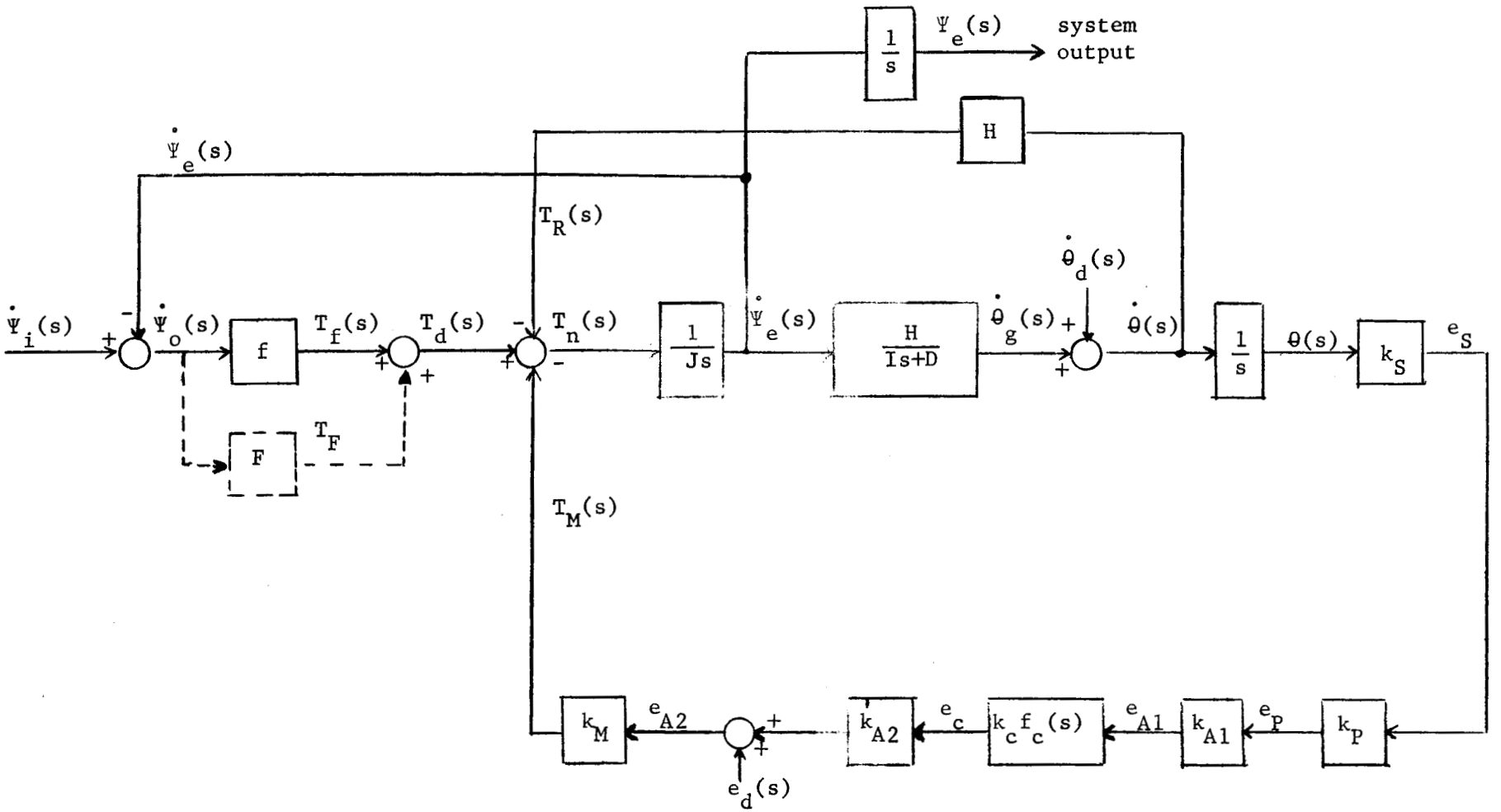

Figure 5. Dynamic Representation of Single-Axis Stabilization Loop

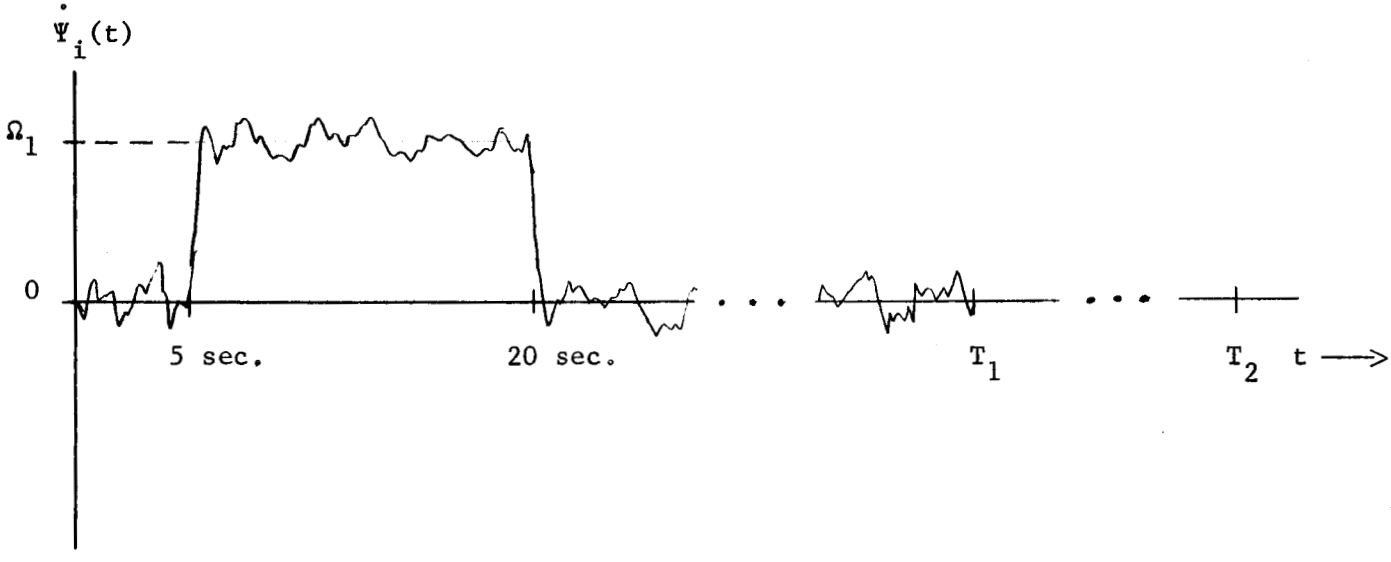

Figure 6. Operational Profile for Vehicle Angular Motion About the W_i Axis

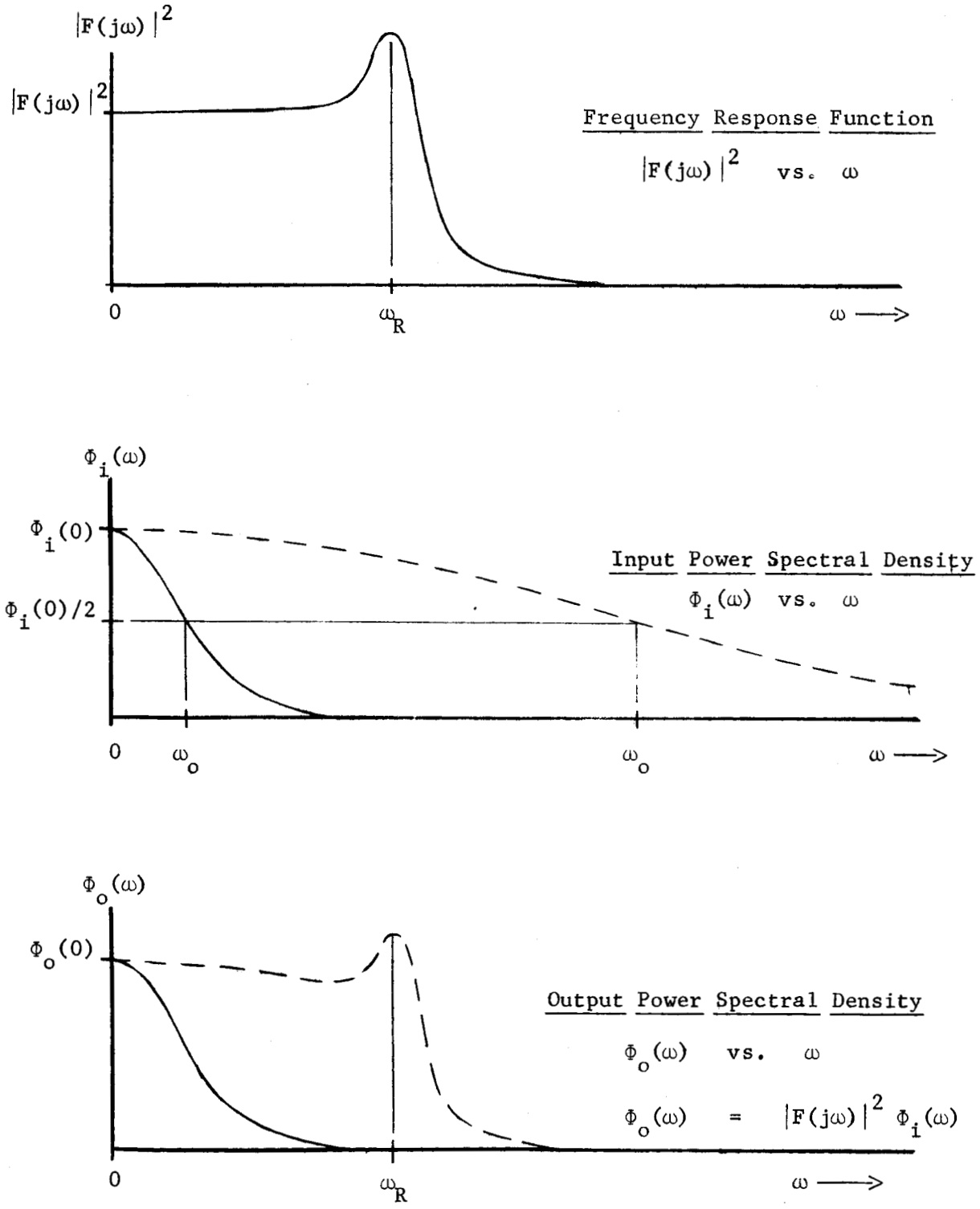

Figure 7. Closed Loop Response of a Linear Feedback System

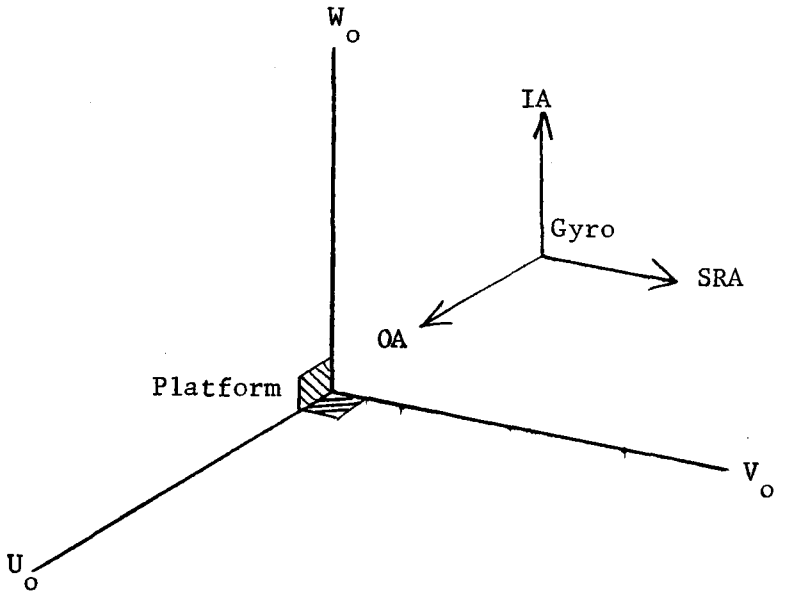

Figure 8. Gyro Orientation in the Platform

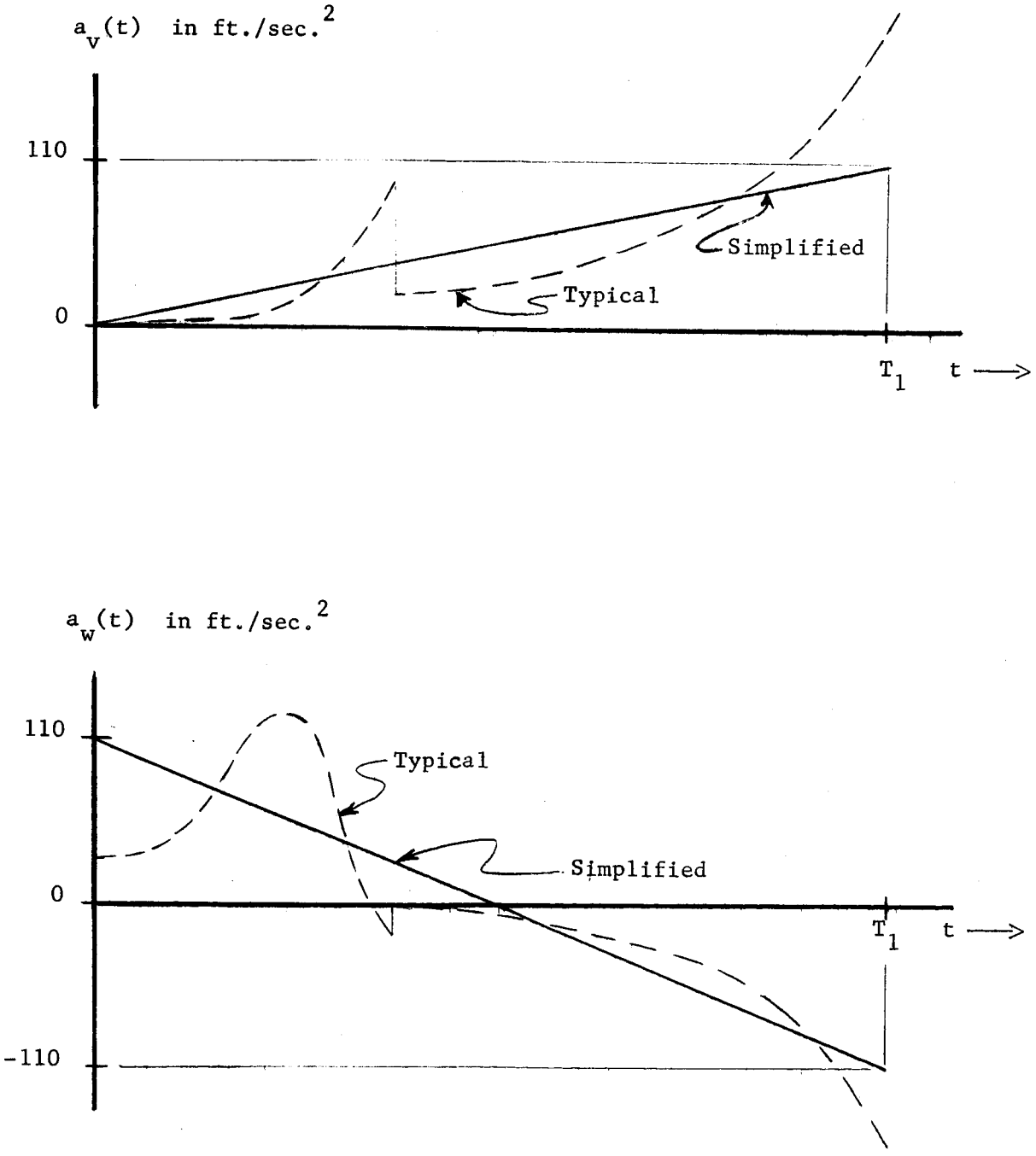

Figure 9. Mission Acceleration Profile

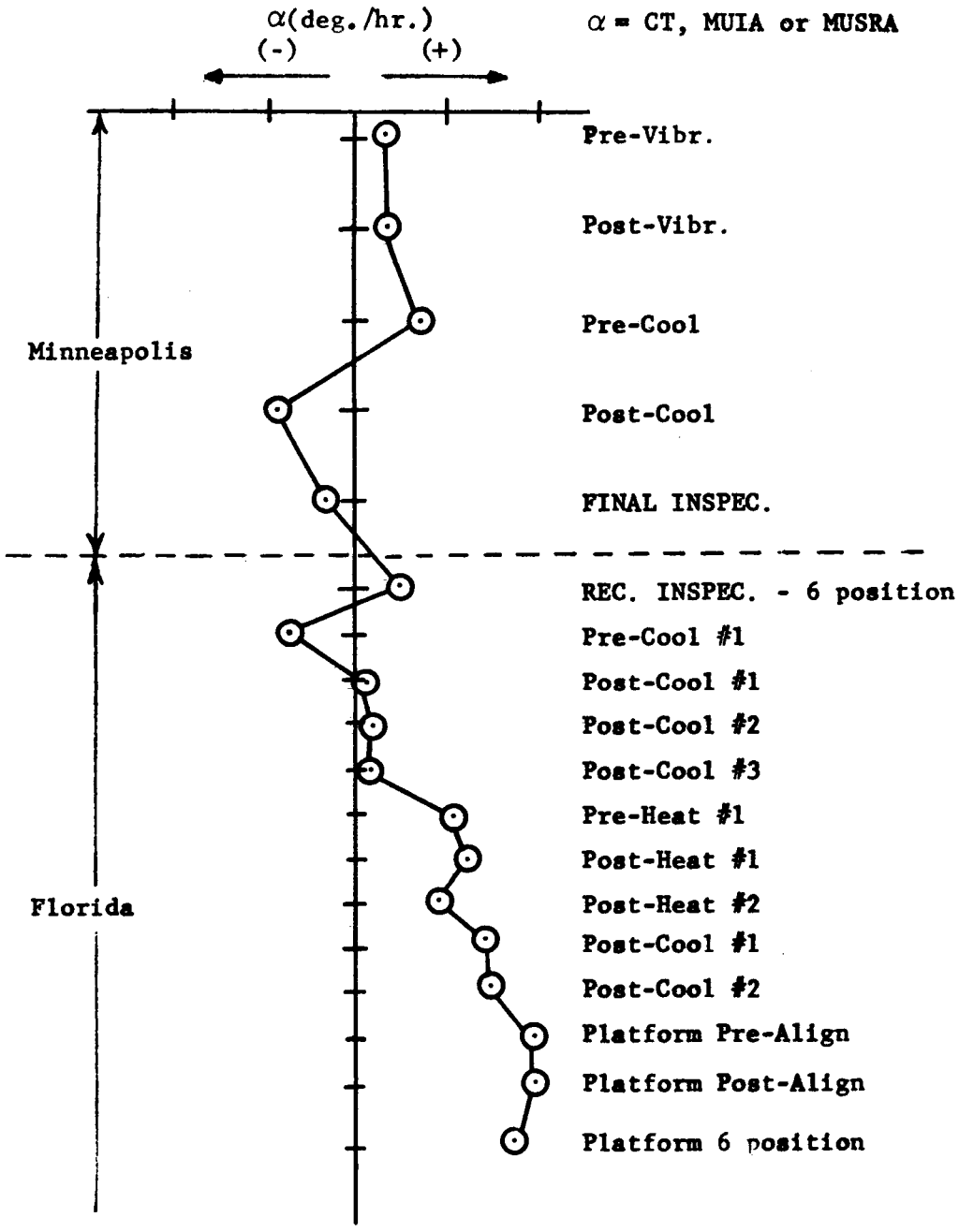

Figure 10. Illustration of Measurements of Gyro Drift Variables CT, MUIA or MUSRA

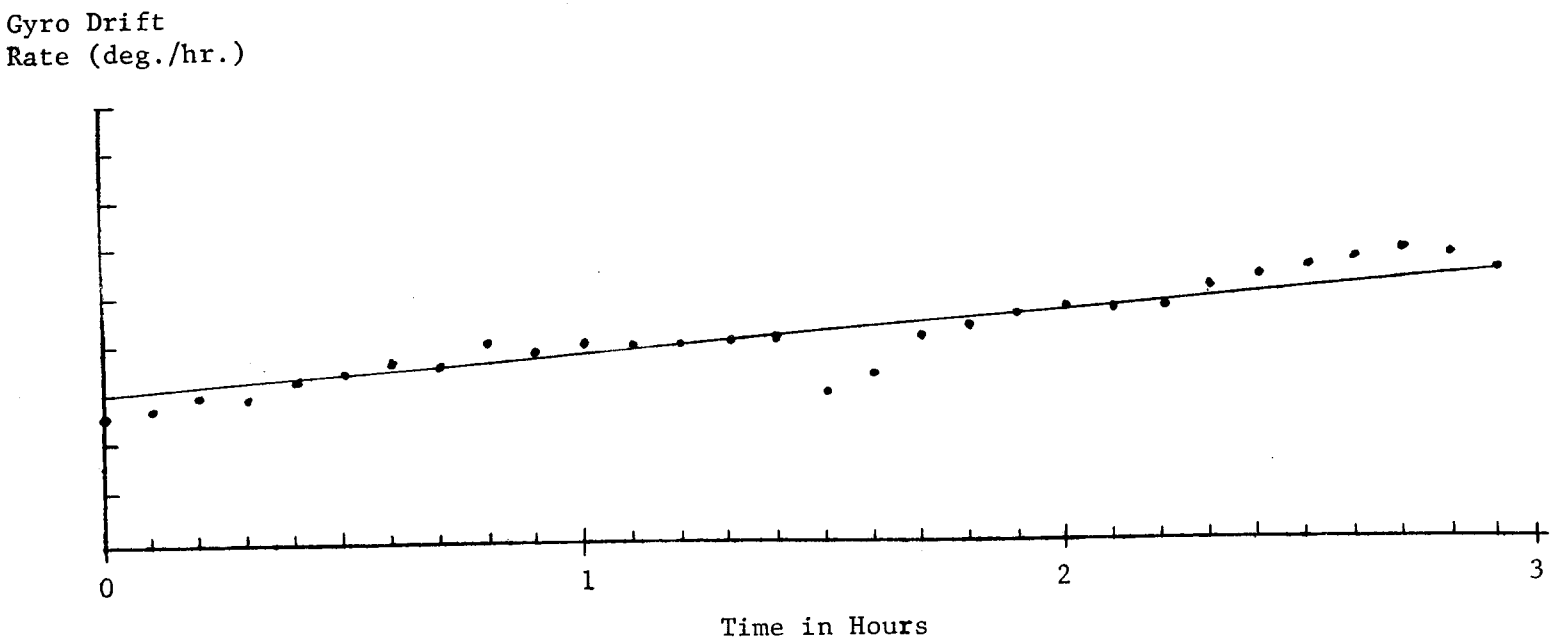

Figure 11. Six Minute Averages of Gyro Drift Rate and a Fitted Trend Line

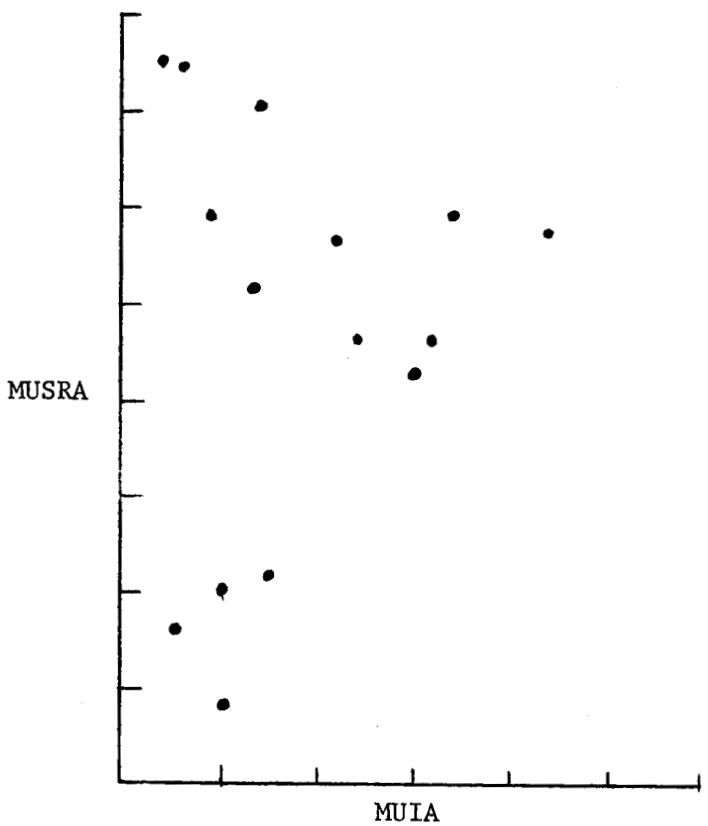

Figure 12. Scatter Plot of MUSRA vs. MUIA for One Gyro

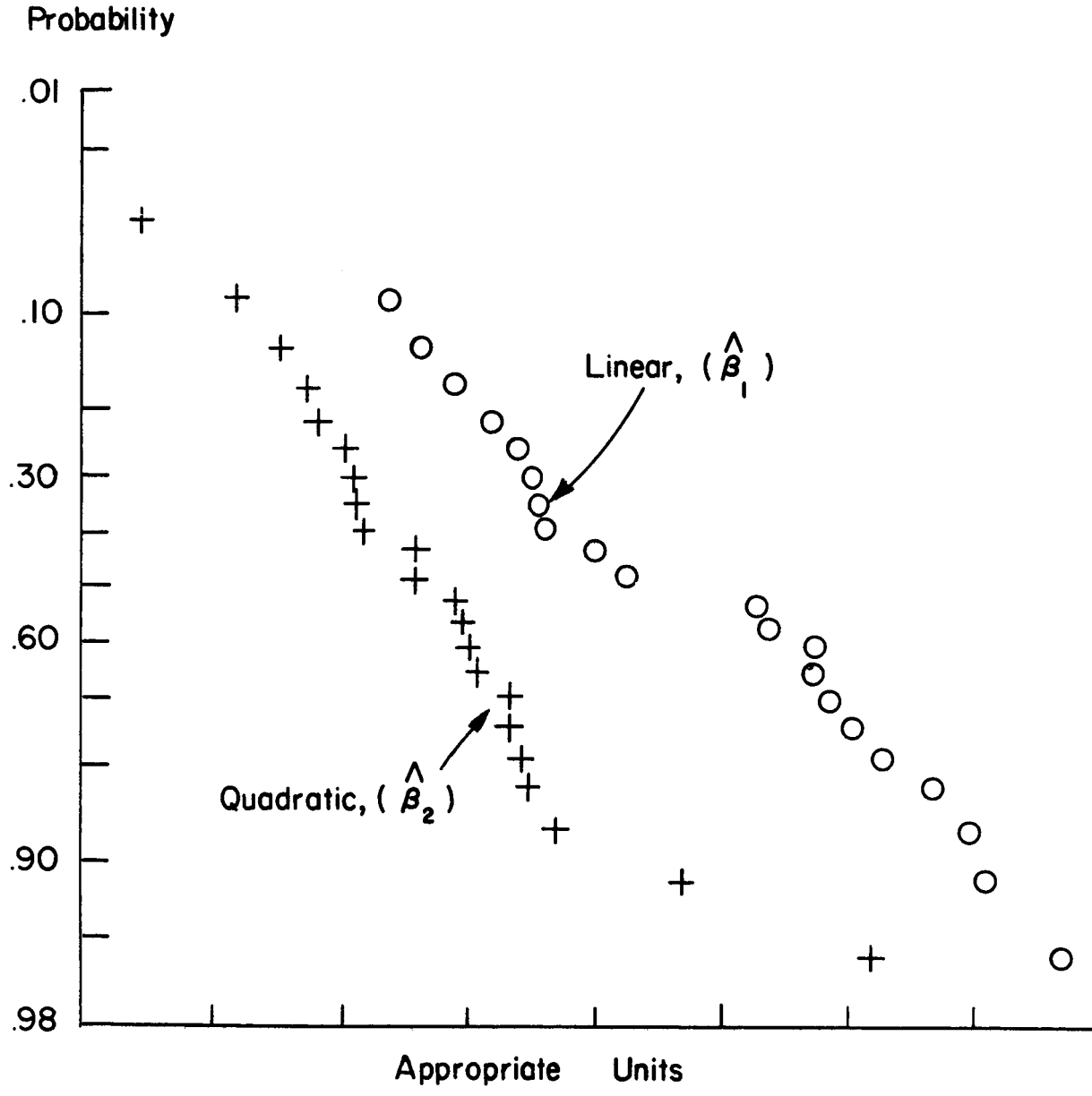

Figure 13. Linear and Quadratic Coefficients, Plotted on Normal Probability Paper.

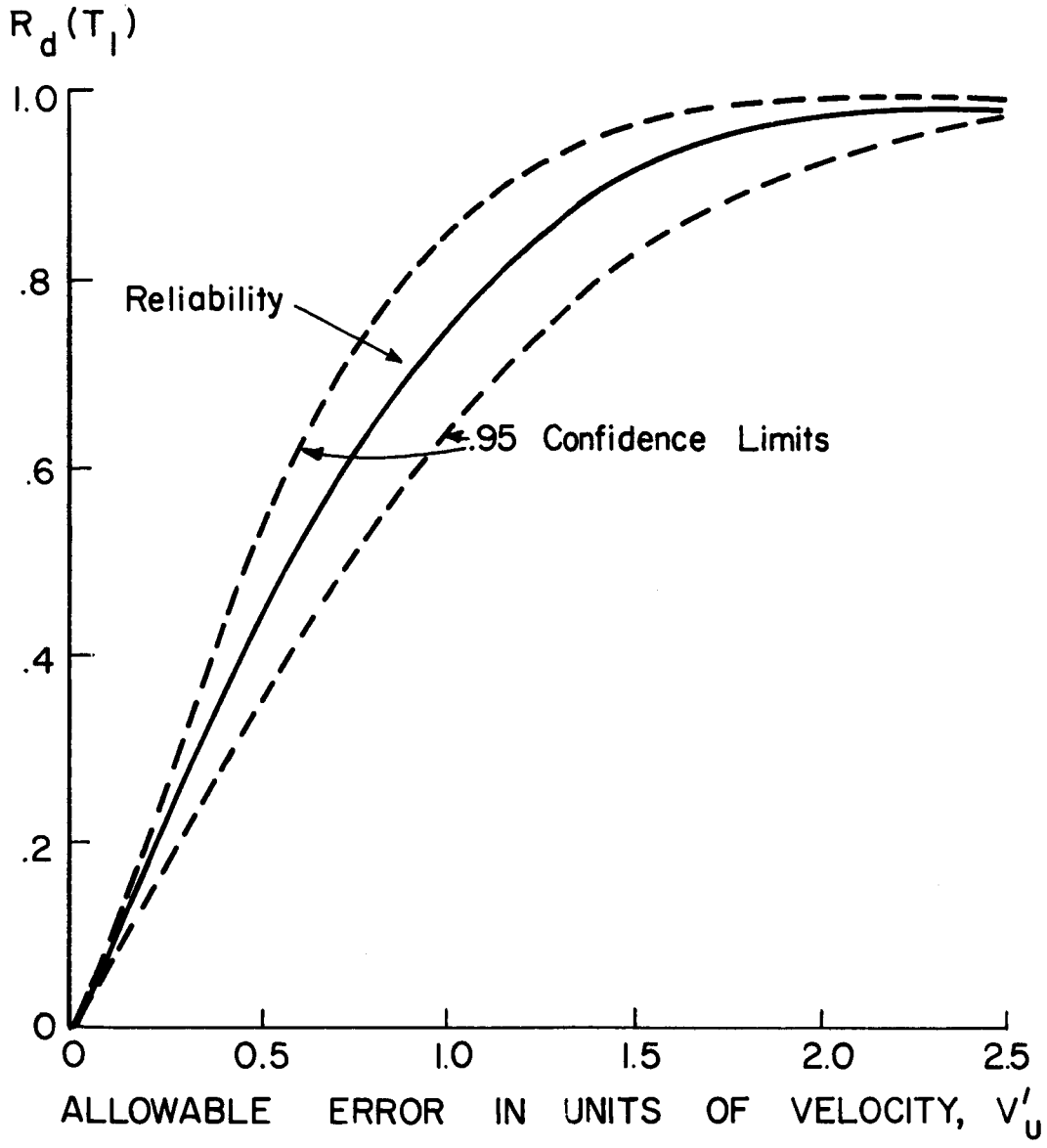

Figure 14. Estimated Drift Reliability, as a Function of the Allowable Error in Velocity at the End of Boost $V_U(T_1)$

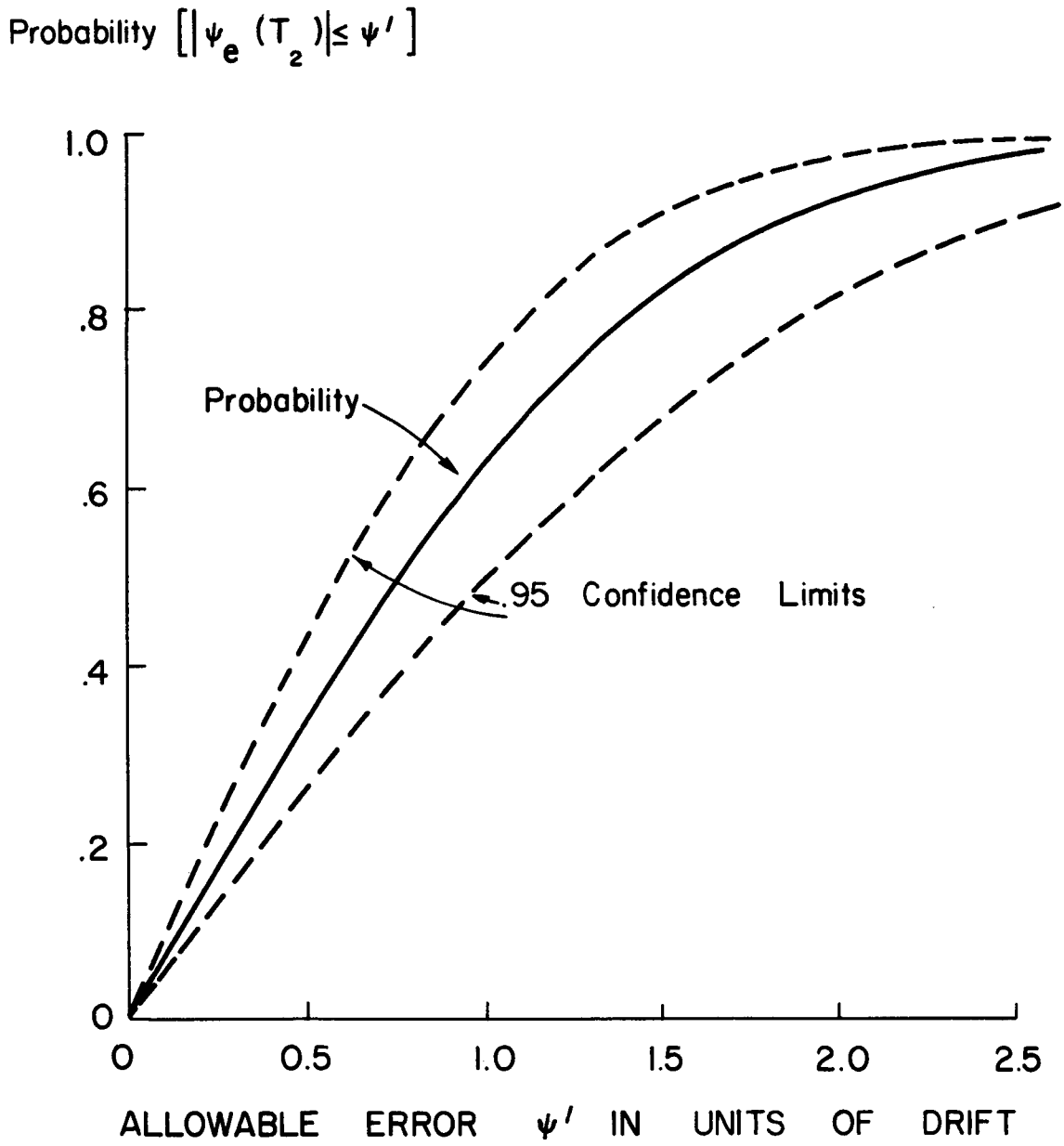

Figure 15. Probability that the Platform Drift is Within the Allowable Error at the End of Orbit.